Novel, tightly structurally related N-myristoyltransferase inhibitors display equally potent yet distinct inhibitory mechanisms

Frédéric Rivière, Cyril Dian, Rémi Dutheil, Paul Monassa, Carmela Giglione, Thierry Meinnel

Novel, tightly structurally-related N-myristoyltransferase inhibitors display equally potent yet distinct inhibitory mechanisms

Frédéric Rivière[iD,a], Cyril Dian[iD,a], Rémi F. Dutheil[iD,a], Paul Monassa[iD,a], Carmela Giglione[iD,@,a,*], Thierry Meinnel[iD,@,a,**]

[a] Université Paris-Saclay, CEA, CNRS, Institute for Integrative Biology of the Cell (I2BC), 91198 Gif-sur-Yvette, France

Running title: Novel NMT inhibition mechanisms

[iD] ORCID 0000-0001-6366-1904 (F. Rivière); 0000-0002-6349-3901 (C. Dian); 0000-0002-2910-6648 (R.F. Dutheil); 0000-0003-4713-8069 (P. Monassa); 0000-0002-7475-1558 (C. Giglione); 0000-0001-5642-8637 (T. Meinnel)
[@]twitter @giglionelab (C. Giglione); @meinnel (T. Meinnel)

[*,**] Corresponding authors; correspondence to thierry.meinnel@i2bc.paris-saclay.fr (lead contact) or carmela.giglione@i2bc.paris-saclay.fr

Keywords: acylation; lysine; myristoylation; *N*-myristoyltransferase; N-terminal modification

Summary

N-myristoyltransferases (NMTs) catalyze essential acylations of N-terminal alpha or epsilon amino groups of glycines or lysines. Here, we reveal that peptides tightly fitting the optimal glycine recognition pattern of human NMTs are potent prodrugs relying on a single-turnover mechanism. Sequence scanning of the inhibitory potency of the series closely reflects NMT glycine substrate specificity rules, with the lead inhibitor blocking myristoylation by NMTs of various species. We further redesigned the series based on the recently recognized lysine-myristoylation mechanism by taking advantage of (i) the optimal peptide chassis and (ii) lysine side chain mimicry with unnatural enantiomers. Unlike the lead series, the inhibitory properties of the new compounds rely on the protonated state of the side chain amine, which stabilizes a salt bridge with the catalytic base at the active site. Our study provides the basis for designing first-in-class NMT inhibitors tailored for infectious diseases and alternative active site targeting.

Introduction

N-myristoyltransferase (NMT) is an essential enzyme in all eukaryotes that ensures protein myristoylation, a major lipid modification [1,2]. Myristoylation usually involves direct ligation of a C:14:0 to the free amino group of N-terminal glycine residues (Gly-myristoylation). NMT has also been shown to mediate lysine myristoylation (Lys-myristoylation) [3,4]. Lys-myristoylation appears to be a rare NMT-driven acylation in humans, and whether it occurs in other organisms is unknown [5]. The lipid donor to NMT is myristoyl coenzyme A (Myr-CoA), and its prior binding is required for the polypeptide substrate to be further properly recognized and then acylated. Release of the products marks the final and limiting step of the reaction [6,7] caused by conformational change and dissociation of CoA. As a result, the myristoylated peptide product is made solvent accessible and fast released from NMT. Due to its poor affinity to NMT and competition with Myr-CoA, a much higher affinity ligand, the Myr-peptide cannot bind again and this ensures enzyme turnover [7-10].

Most Gly-myristoylation targets play indispensable roles in cellular communication, linking cell membranes to extracellular signals and facilitating secretory and endolytic pathways [2]. As such, characterizing the complete set of myristoylated proteins of an organism, its myristoylome, is therefore a long-time goal in the field. Recently, click chemistry approaches have been used to characterize the myristoylome based on myristate mimicking clickable analogs. Such compounds, provided that they are imported into target cells, allow significant enrichment and further characterization of the associated protein (for a review, see [2]). While such analyses can be performed in different organisms and have revealed several unexpected myristoylated proteins [11-15], the click-based approach is still not powerful enough to allow full description of all myristoylated NMT substrates. In addition, false positives may arise through related metabolic pathways [2], mandating the use of NMT inhibitors to validate

the targets identified by click-chemistry [12]. Therefore, nowadays there is still a gap between the expected protein content of an organism and that delivered by even the most sophisticated approaches [2,15,16].

NMT targets are also retrieved from many viral proteomes [2]. Following particle entry, eukaryotic viruses hijack the protein expression machinery to take advantage of cellular NMT activity, as demonstrated for retroviruses including HIV [2,17]. NMT inhibitors have shown efficacy against various viruses including the common cold, polio, and foot-and-mouth viruses without host cell toxicity [18]. More recently, NMT inhibitors were also demonstrated to generate non-infectious particles of SARS-CoV-2 and poxviruses including vaccinia and monkeypox viruses [19,20]. In addition to their use as therapeutics in cancer such as lymphoma [21,22], malaria, and sleeping sickness [11,23-26], NMT inhibitors could therefore be useful in other infections including fungal diseases [27-29].

This study emerged from the observation that an N-terminal glycine-starting peptide extracted from a likely NMT target acts as an inhibitor rather than a substrate *in vitro*. We studied the myristoylation inhibition rules guided by Gly-peptide mimics. This knowledge was used to design Lys-myristoylation-based inhibitors. In both cases, structural and dedicated kinetic analyses revealed the atomic basis of the inhibitory mechanism. Gly-myristoylation inhibition involves product inhibition and single turnover, while Lys-myristoylation inhibition involves a distinct limiting deprotonation step. Finally, armed with our new series of inhibitors, we reveal similar efficacy with a variety of NMTs including those from humans, plants, fungi, and apicomplexa.

Results

Peptides displaying the major recognition motifs are not substrates and behave as tight HsNMT1 inhibitors

We previously reported the very detailed characterization of the substrate specificity of human NMT1 (HsNMT1) for Gly-myristoylation, proposing a canonical optimal substrate logo G_2[NCAQ][CASV][FLC]S[KRC]P[SR] [30]. The sequence that takes each of the most likely residues occurring at a given position of the logo into account corresponds to G_2NCFSKPR, herein referred to as the "reference" sequence. Surprisingly, there was no evidence of the release of myristoylated products of the synthetic peptide displaying the reference sequence upon catalysis by HsNMT1 *in vitro* even at extremely low detection limits (10^{-1} M^{-1} s^{-1}; **Fig. 1a** dotted line). We previously discovered that the first six residues are recognized by dedicated pockets (pockets 2-7) of the active site deep crevice of HsNMT1 [1]. The reference sequence closely resembles the N-terminus of human apoptosis-inducing factor mitochondria-associated 3 protein (AIFM3; Q96NN9, G_2GCFSKPK), differing mainly in the Gly at position 3 instead of Asn. Human AIFM3 is known to be myristoylated, as is the corresponding derived octapeptide *in vitro* [30,31]. In previous reports [30,32], we also observed that the catalytic efficiencies of hundreds of octapeptides derived from genuine substrates range over four orders of magnitude *in vitro* (from 10^1 to 10^5 $M^{-1}s^{-1}$). When comparing the most to the least efficient substrates, we obtained the consensus sequence G_2C[CS][FLT]SKI[RFD] (**Fig. S1**), which was almost superimposable over the reference peptide. Unexpectedly, this sequence lacked the Asn at position 3, like in AIFM3, so we searched for human protein N-termini with the closest similarity to the reference sequence, retrieving only one such sequence - GNLLSKFR - derived from human nuclear pore-associated protein 1 (NPAP1; Q9NZP6), a primate-specific protein [33]. We unexpectedly noticed that the NPAP1-derived octapeptide was not a substrate of either HsNMT1 or HsNMT2 [30] (**Table S1**), similar to the reference peptide.

We next determined the 3D structure of the complex of the reference peptide with HsNMT1 in the presence of Myr-CoA. This peptide substrate was modified into a product, i.e.,

myristoylated, when trapped into crystalline HsNMT1 (**Fig. 2a**; **Fig. S2a**). There was remarkable optimization of the fit of the side chains into major pockets 3 to 6 (**Fig. 2a-c**). The reference peptide proved to be a potent inhibitor, with an IC_{50} of the order of the HsNMT1 concentration used in the assay, indicative of a strong binding constant in the sub-micromolar range (**Fig. 1a,b**; **Table S1**). As an alternative measurement of the binding constant of the reference peptide, we performed microcalorimetry experiments using isothermal titration calorimetry (ITC), measuring a dissociation constant (K_D) of 9 ± 6 nM for the reference peptide when HsNMT1 was pre-incubated in the presence of Myr-CoA (**Fig. 1c**). Without Myr-CoA pre-incubation, the binding constant of the reference peptide was significantly lower, indicating the contribution of Myr-CoA to the binding potency (**Fig. S3a,b**). When the crystal structure of the NPAP1 peptide complexed with HsNMT1 was determined in the presence of Myr-CoA, we also observed transformation of the peptide into the acylated product (**Fig. 2d**; **Fig. S2b**). The associated IC_{50} value was similar to that of the reference peptide (**Table S1**) and the binding constant was in the nanomolar range, similarly to that of the reference peptide.

Upon incubation in the presence of high HsNMT1 concentrations, we observed transformation of the NPAP1 octapeptide into the acylated product induced by HsNMT1 (**Fig. S4**). We hypothesized that peptides such as NPAP1 or the reference peptides behave as prodrug inhibitors through a single-turnover mechanism [34]: once acylated by HsNMT1 in the first reaction round, the myristoylated peptide product cannot dissociate from the enzyme, preventing multiple reaction cycles and hence tightly inhibiting HsNMT1 catalysis. The measured dissociation constants therefore reflect those of the myristoylated product, not simply of the peptide substrate. To examine the actual involvement of the reactive N-terminal group in this process, we assessed the impact of its deletion in the context of the reference peptide (peptide Ac2 in **Fig. 1; Fig. S3c**), which led to a two orders of magnitude decrease in affinity

as assessed using two independent approaches (IC_{50} and ITC, **Fig. 1b, c**). In addition, a single Gly2Ala substitution (Ala2) of the reference peptide led to a two orders of magnitude increase in K_{Dapp} (Ala2, **Fig. 1b**; **Fig. S3d**). These data were in keeping with important involvement of N-terminal amino group reactivity in the binding or the inhibition process. Taken together, the data suggest that the reference peptide and NPAP1 acted as prodrugs.

We next wondered whether other peptides derived from the human proteome (i) not identified as substrates (like NPAP1) or featuring the lowest catalytic efficiencies, and (ii) displaying similarities with the logo could also act as HsNMT1 inhibitors. After screening ~1500 protein N-termini starting with Gly2 in the human proteome, we selected 40 octapeptides from human sequences displaying the closest similarity with the logo at positions 3-7 (i.e., the HsNMT1 binding pockets) and challenged their inhibitory properties. None displayed an IC_{50} value below 10 µM (**Table S1**). As the closest number of similarities of this set at positions 3-7 was 3 out of 5, we concluded that at least 4 similarities - like in NPAP1 and the reference peptide - were required to trigger significant inhibition and potent binding of a given peptide to HsNMT1.

Inhibition of HsNMT1 by the reference peptide was confirmed using a variety of substrates featuring distinct sequences and kinetic constants (G<u>N</u>CVF<u>K</u>GN, GLCT<u>SK</u>PN, G<u>N</u>VI<u>S</u>GGS, GVS<u>FS</u>CPF, GVCC<u>SK</u>GT, GCSV<u>SK</u>KK; **Fig. S5**). We could not fit our data to classic inhibition models (**Fig. S5b-d**), as expected with such an irreversible inhibitor. We focused instead on measuring IC_{50} values (**Fig. S5a**), selecting peptide GCSV<u>SK</u>KK (SOS3) for further systematic analysis and comparison of the inhibition parameters. We derived the binding constant (K_{Dapp}) from kinetic measurements with this peptide to obtain a finer measurement of the binding potency of the most potent inhibitors (**Fig. 1b**).

Structure-activity relationship analysis of the series defines the sequence space leading to tight inhibition

The tight affinity of the reference peptide to HsNMT1 therefore appears to arise from its intrinsic high affinity, which was further entropically increased by its reaction with myristate and subsequent product formation [7]. The dissociation time of the product from the catalyst may be increased by too-high affinity of the product. To probe this hypothesis, we performed a structure-function analysis of the reference sequence, anticipating that decreasing peptide affinity would help release the product and increase the probability of transforming the inhibitor reference peptide into a substrate. Indeed, the NMT catalysis rate constant is limited by the release of the acylated peptide and directly relies on peptide affinity [7]. As a result, the K_m associated with a substrate is usually a direct readout of the associated affinity and determination of the k_{cat} is a direct readout of the off-rate (usually referred as k_5, see [35]). In this regard, we could check that an already N-myristoylated reference peptide (Myr-GNCFSKPR) did not behave as an effective inhibitor of HsNMT1 ($K_{D\text{app}}$ >10 µM). This data is in line with a very low backward on-rate (k_{-5}) of the free reaction product (see also *Introduction*).

We first extended the sequence length of the reference peptide by C-terminal amidation and with one or two additional Ala residues (**Fig. 1a**). The longer peptides were still inhibitors and the K_D values reaching one nanomolar with two additional Ala residues (**Fig. 1c,d**; **Fig. S3e-h**). The crystal structure of the amidated peptide complexed to HsNMT1 revealed a hydrogen bonding interaction involving both the NH and the C-terminal amides of Arg9 of the reference peptide ligand and the protein backbone carbonyl group of residue Ile469 of HsNMT1 (**Fig. 2e**; **Fig. S2c**). Interestingly, a reference peptide featuring a five-residue C-terminal extension (V_{10}PTLK$_{14}$) did not improve the binding potency compared with the reference peptide (**Fig. 1b**). Indeed, the associated crystal structure of the complex with

HsNMT1 indicated that the additional amino acids in the peptide did not promote novel interactions with the enzyme's outer surface beyond the Arg9 residue (**Fig. 2f**; **Fig. S2e**). We concluded that most of the binding properties of the series were contained within residues 2-9.

We next studied the effects of progressive deletions of the reference peptide. When shortened by more than one residue at the C-terminus, the reference peptide was no longer a potent inhibitor and behaved as a substrate (dashed line in **Fig. 1a**). Previous data demonstrate a crucial role for Ser6Lys7 in efficient NMT catalysis [30]. Even so, the short tetrapeptide GNCF was a highly efficient substrate (**Fig. 1a**), suggesting that Asn3 provides sufficient affinity to allow efficient Gly-myristoylation and does not require any other specific residues beyond Phe5. We concluded that there are two major sources of peptide affinity: (i) the N-terminal part of the peptide featuring critical aa3 (aa2-5), optimal with Asn; and (ii) the C-terminal side chain featuring Ser6Lys7 (aa6-9). Residue 5 appeared to be important, likely to orientate aa3 properly into the corresponding binding pocket. The C-terminal part beyond residue 7 also played a role but to a lesser extent, as exemplified by the interaction networks related to the crystal structure of HsNMT1 in complex with the Pro8Ala variant of the reference peptide (**Fig. S2d**).

To probe the impact of each residue of the octapeptide on NMT catalysis and inhibition, single changes were sequentially introduced at positions 3 to 9 of the reference peptide. Alanine scanning revealed that changes to positions 2-7 of the reference peptide turned them all into substrates, unlike positions 8-9 (**Fig. 1d**). These data fully complement the reference peptide deletion analysis and confirm a central role for residues 2-7 (**Fig. 1a**).

To better assess the sequence space around the reference peptide as an inhibitor, a set of >30 additional peptide variants with single substitutions other than Ala were designed and challenged with HsNMT1 (**Fig. 1d**; **Fig. S3i-m**). Again, the majority of changes converted the reference peptide inhibitor into an HsNMT1 substrate, while only a few mostly conservative

(i.e., chemically related) substitutions maintained the inhibitory behavior. The Gly2 substitution space was investigated with Ala2 and β-Ala2 changes, both of which added an extra methyl/methylene group on either the side or main chain and converted the reference peptide into a substrate, but with only very poor efficiency for Ala (**Fig. 1d**). The Ala2 variant was a poor inhibitor with an inhibition constant in the micromolar range (**Fig. 1b,c**). To promote inhibition only, both Asn3 and Ser6 appeared to be irreplaceable by any other amino acid, while position 5 required either (i) a very hydrophobic residue such as Leu, Tyr, or Phe, or (ii) a residue with an amide group such as Asn or Gln (**Fig. 1d**). Position 4 could only be substituted by short polar residues including Cys and Ser to prevent the variants behaving as substrates (**Fig. 1d**). The catalytic efficiencies associated with the non-inhibiting, substrate variants were usually of the same order of magnitude as those of the best substrates and several orders of magnitude higher than those associated with inhibition alone (**Fig. 1d**). As a result, such variants with efficient catalytic properties were disregarded as they did not match the specifications of inhibitors, which must remain stable over time. Substitutions leading to substrate behavior were also associated with a significant increase in the inhibition constant. Finally, we noticed that this analysis could be considered a readout of unfavorable residues leading to Gly-myristoylation. Indeed, a substitution reverting the inhibitor into a substrate indicated that it likely decreased the binding potency to such an extent that it made catalysis easier by significantly increasing the turnover number. Because the limiting step is product release, this indicated a relaxed binding potency of the peptide. Starting with a peptide with very high affinity, any decrease in binding was expected to favor improved catalytic performance, as assessed by catalytic efficiency. Therefore, the higher the k_{cat}/K_m resulting from a substitution, the more unfavorable HsNMT1 binding to the residue. This was the case for Lys3- or Leu6-containing derivatives, which are known to need an almost perfect match to

the reference peptide to promote Gly-myristoylation [30]. This readout from a synthetic reference peptide sequence mirrors the analysis of those sequences compiled from existing proteins which are or are not HsNMT1substrates (see [30]).

The consensus motifs of NMTs (GC[CS][FLT]SKI[RFD] for the best substrates or G[NCAQ][CASV][FLC]S[KRC] for the overall set) are biased by extra Cys residues that do not influence NMT-driven Gly-myristoylation but rather S-palmitoylation, a modification governed by palmitoyltransferases that relies on previous Gly-myristoylation [30]. In our current analysis, a consensus sequence GN[CS][FLYNQ]SK[RP][RA] emerged, which closely mimicked that obtained from our previous kinetic analysis of peptides arising from natural sequences [30]. The analysis confirmed the unique roles played by Asn3 and the Ser6Lys7 motif in high affinity interactions. Of note, position 4 appears to favor small hydrophilic residues, while position 5 better supports bulky side chains.

Gly-myristoylation therefore appears to involve two sets of ligands, those containing Asn3 and those with Ser6Lys7. Simultaneous inclusion of both features leads to deleterious, distorted effects in terms of catalytic turnover, as demonstrated by the strong inhibitory behavior of the reference peptide. We retained G_2NSFSKPR (Ser4) as the chassis sequence for downstream analysis, thereby avoiding issues related to manipulation of Cys-containing peptides like the reference peptide.

Lys-myristoylation-inspired design of potent HsNMT1 inhibitors allows substitution of the reactive amino group with non-natural residues

The Gly2Asn3 head group therefore appeared to be very difficult to modify into a closely related di-amino acid to obtain a compound as potent as the reference peptide. We recently showed that NMT can react with the side-chain of a Lys residue, provided it is properly

positioned at the N-terminus and not preceded by a Gly, which is more reactive [5]. Interestingly, we noticed that the structure of the complex of HsNMT1 with the *ac*Lys peptide N-terminal group (*ac*-KSFSKPR, *ac*K) was very similar to that of the reference peptide (**Fig. 3a,b**). While the *ac*Lys-starting peptide was a substrate of Lys-myristoylation, we wondered whether we could design Lys-myristoylation inhibitors based on both the reference peptide chassis and the acetylated lysine group to remove the non-substitutable Gly2Asn3 group. In addition to acetylation (*ac*), we have shown that several substitutions of Gly2 make it possible to favor Lys3 myristoylation, including Gly2Ala and *ac*Gly (see Ref [5]).

We first used synthetic lysine mimics to assess the effects of side-chain length. We shortened the basic side chain of lysine to ornithine (Orn, reduced by one CH_2), di-amino butyrate (Dab, reduced by two CH_2s), and di-amino propionate (Dap, short basic chain CH_2NH_2) in combination with various Gly2 substitutions (*ac*, *ac*G, A). *ac*[Orn], *ac*[Dap], A[Orn], and *ac*G[Dab] did not undergo myristoylation even at the highest HsNMT1 concentrations (**Table 1**), unlike their close homologs, *ac*K, AK, *ac*GK and *ac*G[Orn]. We hypothesized that such non-reactive compounds might act as HsNMT1 inhibitors. While the *ac*[Dap] derivative was a poor inhibitor with an inhibition constant of 11 ± 1 µM, the *ac*[Orn] derivative showed an order of magnitude higher affinity (**Fig. 4a**), suggesting that the N-terminal reactive amino group – if properly aligned with the α-carbon through 2-3 carbon bonds like in Orn or Dab – might contribute to binding while not promoting catalysis. This encouraged us to further design and study compounds with N-terminal Orn and Dab variations based on the GK sequence.

We first assessed *ac*G[Dab], [Dab], and A[Orn], all of which acted as potent competitive inhibitors with IC_{50} values of the order of the HsNMT1 concentration used in the

assay. This indicated a tight binding constant in the low micromolar range (i.e., <0.4 µM; **Fig. 4a**). Dab and Orn but not Lys clearly led to strong inhibition.

To modify the amino group orientation towards the catalytic base and to mimic the Gly-myristoylation-producing mechanism, we built two D-Orn derivatives: the enantiomeric stereoisomer of L-Orn (**Fig. 4b**; symmetric branching of R_1 and R_2 with respect to Cα3) either with *ac* or *ac*G to optimize the filling of pocket 3. Interestingly, the *ac*[D-Orn] N-terminal group was a remarkably close mimic of the GlyAsn dipeptide, like in the reference peptide (**Fig. 3a,c**; **Fig. S2a,f,g**), while our previous work revealed that Asn is favored in pocket 3 [1,30]. Both D-Orn derivatives were potent inhibitors, especially the *ac* version (K_D=50 nM). A similar result was observed with *ac*[D-Dab] and A[D-Orn] derivatives (**Fig. 4a**), and *ac*G[D-Orn], G[D-Orn], and [D-Orn] derivatives were also strong inhibitors but to a lesser extent than *ac*[D-Orn]. When *ac*[D-Orn] was installed on the NCS1-derived chassis – i.e., a non-optimal Lys-myristoylation chassis without a hydrophobic position at position 5 – significant, though weak, myristoylation was observed (**Table 1**). This indicated that potent inhibition was only possible with an optimal fit for Lys-myristoylation, including a hydrophobic residue filling pocket 5.

The partition ratio *r* is defined as the value of the intersection minus 1 of the residual enzyme E activity in function [I]/[E]. The *r* ratio defines the average number of turnover events required to form a catalytically inactive enzyme ”E” in the presence of an inhibitor “I” [36]. D-Dab or D-Orn derivatives of the *ac* series both had partition ratios of 1.5 (**Fig. 4c**), indicative of very high inactivation efficiency with an inhibition on-rate similar to that of the off-rate. Moreover, the partition coefficient of the corresponding variant of the reference peptide series (Ser4) was 3 instead of 1.5 for *ac*[D-Orn], indicative of an improved binding constant for the Lys-myristoylation series compared with the previous one (**Fig. 4c**).

Finally, we obtained the crystal structure of [Dab] and *ac*[D-Orn] in complex with HsNMT1 and retrieved the complex without conversion of the substrate into a product (**Fig. 4d-g; Fig. S2f,g; Fig. S6a,b**). The complex featured direct binding of the D-Orn and Dab amino groups to the carboxy terminal base. The reactive amino group of the Dab side chain bonded directly with the carboxy-terminal base of HsNMT1 (**Fig. 4f,g; Fig. S2f,g**). Such direct bonding of the reactive amino group of both inhibitors was unlike the efficient GK peptide, which requires water-mediated binding and acylation [5]. This salt bridging was identical to the binding of the *ac*K and AK Lys-myristoylation substrate derivatives (**Fig. 3c,d**). This direct salt bridge created in the context of the D-Orn or Dab side chains, which leads to optimal sizing, is expected to be stronger than the one made with Lys and at least 100-fold less prone to reaction. This likely explains the lower reactivity and behavior of the D-Orn series as potent inhibitors. Both compounds bound to Thr282 (**Fig. 4d-g**). The non-acetylated Dab compound featured a water network within pocket 3, indicative of less bonding than both acetyl derivatives, perhaps explaining its lower binding constant (**Fig. 4f**).

In conclusion, (i) the chain length bringing the reactive amino group, (ii) the chiral conformation of the substituents R_1 and R_2 of the Cα group facing pocket 3 (Cα3; **Fig. 3**, and **Fig. 4b**), and (iii) the optimal occupation of pocket 3 with a moderately bulky N-terminal moiety mimicking Asn were mandatory for effective Lys-myristoylation-based design of HsNMT1 inhibitors.

pH-dependent Lys-myristoylation is indicative of a different inhibition mechanism to Gly-myristoylation

Crystal structures of Gly-myristoylation-inspired NMT inhibitor complexes always revealed conversion of the peptide into the product, indicative of prodrug inhibitors [5,6,30]. The crystal

structures of the two potent inhibitors *ac*[D-Orn] and [Dab] did not reveal myristoyl group reactivity with the peptide. In contrast, the 3D structure obtained with the Lys-myristoylation substrate *ac*G-[Orn] after crystallization growth performed under identical conditions did show acylation [5]. We hypothesized that the potency of the second series was mostly related to the strong salt bridge between the amino group of the lysine homolog side-chains and the carboxy-terminal base of HsNMT1. The pKa of the Lys amino reactive group and the unnatural mimics like Orn, Dab, or Dap is indeed expected to be high (>10.5) and, under physiological pH, only a very small fraction is uncharged (0.01% at pH 7.5).

We investigated whether the uncharged form corresponded to the actual reactive compound. We compared the effects of both the Gly-myristoylation and Lys-myristoylation series at pH 7.5 and 9.0, i.e., the pH range compatible with assay conditions, by measuring the catalytic efficiency of myristoylation by HsNMT1 (**Fig. 5a**; **Fig. S7a,b**). The Gly-myristoylation series was fully independent of pH regardless of peptide sequence (ARF6, GK, SOS3). This indicated that Gly-myristoylation could be achieved with the same efficiency by either deprotonation of the alpha amino group of Gly or by bypassing deprotonation. As the pKa of the alpha amino group of Gly is ~7.7 and the pH of the cell is ~7.2, the prominent physiological form corresponds to the positively-charged form (see dashed line in **Fig. 5a**), which requires NMT-catalyzed deprotonation before reaction. The enzyme-catalyzed deprotonation step is probably therefore not rate-limiting, as expected from the kinetic model, which shows very high catalytic rates (k_4) compared with the overall rate, which is limited by dissociation [7] (**Fig. 6a**).

We next investigated the influence of pH on the Lys-myristoylation peptide substrates using two acetylated peptides derivatives, also from the ARF and GK series (*ac*ARF6, *a*cGK). The data were different to the Gly-myristoylation series (**Fig. 5b**; **Fig. S7c,d**). In addition to

low rates of Lys-myristoylation involving k_{cat} values two orders of magnitude lower than those of Gly-myristoylation (0.001 *vs* 0.1 s^{-1} **Table 1**), there was strong pH dependence and the increase in catalytic efficiency closely mirrored increases in the non-protonated form (**Fig. 5b**). The same pH dependence of Lys-myristoylation was confirmed with AK substrates derived from ARF and the reference peptides (**Fig. S8a**). We concluded that the mechanism of Lys-myristoylation by HsNMT1 exploited the non-protonated version of the peptide. The deprotonated peptide was only very poorly abundant within this pH range, suggesting that only a small fraction (<0.1%) of the substrate is available for catalysis. As a result, one can deduce that the rate of acylation catalysis in the Lys-myristoylation reaction ($k_4 > k_{cat}/0.1\% = 10\ s^{-1}$) is very similar to that of the Gly-myristoylation reaction (16 s^{-1}; **Fig. 6**).

These data strongly suggested that the mechanism of inhibition of the Lys-myristoylation-inspired peptides involved the protonated version (**Fig. 6b**). Interestingly, this form is expected to predominate at physiological pH (**Fig. 5b**, **Fig. S8b**). This balance favoring the charged species suggests an inhibition mechanism where Lys-myristoylation-inspired compounds exert their inhibitory effect primarily through stabilization of the salt bridge created in the ternary complex ("salt bridge inhibition pathway" in **Fig. 6b**). This contrasts with the Gly-myristoylation-inspired inhibitors, which exert their inhibition solely through conversion of the peptide into a product that remains strongly bound to the enzyme due to their high affinity ("product-driven inhibition" in **Fig. 6a**). Nevertheless, one cannot formally exclude that the very small proportion of deprotonated peptides may lead to myristoylation, as is the case with the substrate peptide of the similar Lys-myristoylation series already identified [5]. If so, the most potent ligands, such as those of the D-Orn series, should behave as potent prodrug inhibitors, similar to Gly-myristoylation inhibitors. The mechanism shown in **Fig. 6b** takes this putative secondary effect into account, which can be considered an inhibitor "rescue step", with the

involvement of an alternative inhibitory step ("product-driven inhibition"). Product formation of this series is unlikely to involve the deprotonated form arising from the salt bridge, since direct deprotonation of the salt bridge is most unlikely to occur, as it systematically involves a water-mediated interaction with the catalytic base considering all known mechanisms reported to date for the GNAT family of acyltransferases [37]. In the model (**Fig. 6b**), there would therefore be two inhibited stages with two inhibitory forms, the major one corresponding to the enzyme-substrate complex and the minor one to the enzyme:product complex. This dual inhibition promotes a virtual balance favoring tight inhibition, as assessed by the remarkably low partition ratio of the series (**Fig. 4c**). Since the enzyme-substrate complex can dissociate with an off dissociation rate (k_{-1} step in **Fig. 6b**) an order of magnitude higher than that of the enzyme product dissociation (k_5 step in **Fig. 6b**), it is not unlikely that this inhibition eventually leads to progressive, extremely slow rebalancing of the equilibrium towards the enzyme:product form, which could even eventually become dominant (**Fig. 6b**).

Salt bridging with the catalytic base is a common mechanism of potent inhibition of NMTs

We superimposed the 3D structures of HsNMT1 bound to the lead peptides (i.e. both reference and *ac*[D-Orn]) of our two series based on an optimal peptide binding motif to those corresponding to each of three already described main leads (SC-58272 [38], DDD85646 [23], and IMP-1088 [18]) displaying high affinity for NMTs (**Fig. 7a**). PCLX-001, an effective NMT inhibitor in cancer [21,39,40], was not included in the comparison. Notably, it closely resembles DDD85646, differing only in a substitution of the active-site distant pyrazole ring, and its 3D structure in complex with the target is unavailable. The binding of our series perfectly matched that of the other compounds, all of which similarly occupy the NMT peptide binding site (**Fig.**

7a). The crystal structure of SC-58272 with *Saccharomyces cerevisiae* NMT reveals a direct interaction and salt bridging of the protonated amino group Nγ with the carboxy terminus base of Leu455 (d_{N-O} 3.1 Å with each O, PDB Id 2NMT[38]). Similarly, DDD85646 and IMP-1088 also salt bridge with the carboxylic base guaranteed by their respective dimethylamino and piperazine groups (d_{N-O} of 2.9 Å and 2.7 Å, respectively; **Fig. S9a,b**), such groups displaying pK values of the order of 9.8. Because our Lys-myristoylation series was identified through fully independent approaches, we conclude that tight inhibition to NMT without catalysis involves similar binding mechanisms.

Of our two series, the initial series based on Gly-myristoylation mimicry is unique as it does not take advantage of the salt bridge but rather the catalytic pathway (**Fig. 6a**). We noticed that each of these three small compounds inhibited several NMTs, including fungus and parasite NMTs. We therefore wondered if the reference series not involving a salt bridge could also inhibit NMTs other than HsNMT1. To test this, we focused on a selection of NMTs each recapitulating a type of NMT sequence and eukaryotic diversity (see phylogenetic analysis in Refs [1,2]). We first confirmed that HsNMT2 was also potently inhibited with similar inhibition binding constants (**Fig. 7b**). We next examined the plant *A. thaliana* NMT (AtNMT), and again observed potent inhibition. Finally, we challenged two further NMTs from unicellular eukaryotes, the apicomplexan *Plasmodium falciparum* (PfNMT) (which causes malaria) and the yeast *Saccharomyces cerevisiae* (ScNMT) [41]. Remarkably, potent inhibition was observed in both cases (**Fig. 7b**). We concluded that optimal substrate mimicry was a relevant alternative to salt bridging inhibition to inhibit NMTs.

Discussion

The amino terminal salt bridge is a key structural element common to potent NMT inhibitors

The search for potent NMT inhibitors has taken advantage of peptidomimetics combining (i) mimicry with the best substrates known at the time (yeast Arf2p); (ii) N-terminal Gly to Ala substitution to prevent the reaction (yielding ALYASKLS-NH_2); (iii) redesign of the amino terminal tripeptide to an alkyl chain of varying length; and (iv) altering the N-terminal amino group into imidazole derivatives [42-46]. All the lead compounds, including the 2-methyl imidazole substitution of the semi-peptidic compound SC-58272, display in common (i) a chemical group ensuring a protonated N-terminus; (ii) Ser6 and Lys7 side chains or nonpeptidic mimics of both; and (ii) inhibition constants in the sub-micromolar range. Provided the distance between these crucial groups ensures the salt bridge, the best compounds originating from this approach behave as moderately potent and specific NMT inhibitors.

Screening strategies supported by medicinal chemistry approaches have identified new classes of NMT inhibitors [47], including potent, nanomolar inhibitors with effects against infections caused by *Trypanosoma brucei*, *Leishmania donovani*, and *P. falciparum* [11,18,23,48-50]. These include the most effective NMT inhibitors reported to date, IMP-1088 [18] and DDD85646 [23]. Structural approaches indicate that all known compounds inhibit by direct competition only with the peptide-binding site (**Fig. 7a**). While belonging to distinct chemical families, IMP-1088 and DDD85646 display common interaction features (**Fig. S9a**): salt bridging with the carboxylic base guaranteed by their respective dimethylamino and piperazine groups, and deep entry into pocket 5 with hydrogen bonds (d_{N-O} 2.9 Å) between Ser405 and their common distal pyrazole groups [51]. Interestingly, though Ser405 is well conserved amongst NMTs, it is substituted with a Leu (L334) in fungi such as *S. cerevisiae*, which would be expected to clash with the pyrazole group and prevent the hydrogen bonding interaction in

fungal NMTs (**Fig. S9b**). Our compounds favor either a stacking interaction between the two hydrophobic groups of each partner or a hydrogen bond induced by inhibitor residues featuring an amide group, most likely with Ser405 of HsNMT1. Unlike the peptide mimics described in this study featuring a hydrophobic residue at position 5, the small compounds of the IMP or DDD series or those with an amide group at position 5 of our series are therefore not expected to inhibit fungal NMTs.

Remarkably, the potency of both of our substrate-inspired series also depends on the interaction between the C-terminal carboxyl group of Gln496 through the primary amino group of either a lysine or the N-terminal group for Gly2. Interestingly, the Lys-myristoylation series forms a salt bridge similar to the IMP and DDD series. Like the previous series, the hydrophobic character of the group entering pocket 5 is also prominent, but there is no interaction with Ser405, which is located within 3.6 Å of the phenyl ring (PDB Id 6QRM, $d_{O\text{-}C}$). Instead, the distal interactions with pockets 6 and 7 – which do not occur with IMP-1088 and DDD85646 - are strong enough to trigger the potency as demonstrated, for instance, in the deletion analysis. Either the Ser405 hydrogen bonding with the small compounds or the Lys6 salt bridging with the peptidometic series promote the closure of the ab-loop, which protects the compounds from premature release (i.e., the interaction decreases the off rate). Of note, the ab-loop closure stabilization includes another Lys107-Asp184 internal salt bridge (see Supplementary Figure 14 in Ref. [6]). Clearly, all series described to date exert their potency through very similar mechanisms involving both the catalytic base and ab-loop closure as triggered by a more distant interaction. Respect of the distance between the two elements is also important, as evidenced either by the fragment-based design of IMP-1088 made through ligation between IMP-772 and IMP-358 or by the random screening of a sub-library from the original DDD64558 pyrazole hit to generate DDD85646 [18,23]. Taking everything into account,

these compounds bear a striking resemblance in terms of their spatial occupancy within the active site peptide pocket. Our series and IMP-1088 both take advantage of pocket 3 either filled with the N-terminal acetyl moiety or two hexyl groups, respectively (**Fig. S9c,d**). We previously confirmed a large space in this pocket which may even be filled with two linear amino acids or one as large as methionine [5]. However, the inhibitory properties of our series appear poorly compatible with larger chains better mimicking IMP-1088 in this pocket (**Fig. 1d**). This probably relates to the interaction with the catalytic base (Gln496) and how both the length and the angle are altered by the overall restraints on the main backbone. Our series brings additional constraints due to filling pockets 6 and 7, unlike IMP-1088. Finally, while outside the peptide binding site, positions 8 and 9 also contribute to the binding, with several side chains inducing destabilization of the resulting complex (**Fig. 1d**).

Role of the protonability of the amino terminal group in overall NMT catalysis and inhibition

The alpha amino terminal group of proteins (Nα) is a frequent site of protein reactivity and associated modifications. It is also the most diverse site, with 82 distinct modifications described to date ranging from -89 Da to +738 Da [52,53]. This high reactivity is not only due to it being the first common reactive group to emerge from the ribosomal tunnel during protein synthesis but also because N-termini are >80% solvent exposed [54] and because the neutral pK of the alpha amino group (7.7 ± 0.5 [55]) is close to the intracellular pH (7.2 ± 0.2). Easy enzyme-mediated deprotonation makes the alpha amino group behave as a nucleophile and react with a variety of donors – N-acetyl in the first place – to create various bonds. The protonability and acidobasic character of the primary amine are lost upon amide bond creation by formylation, acetylation, or fatty acylation.

Recent data have revealed a Gly-myristoylation mechanism for NMT and the importance of a water channel and water-mediated bond of the N-terminal alpha group of Gly to the C-terminal carboxyl group (Gln496), which acts as catalytic base promoting deprotonation and further catalytic reactivity [1,6]. Here we show that, with respect to Gly-myristoylation, NMT catalysis proceeds as efficiently with either protonated or deprotonated alpha amino group peptide substrates. This arises from the very efficient NMT deprotonation rate, which is not limiting with respect to the other steps of catalysis. NMT can also catalyze Lys-myristoylation on a series of N-substituted model targets, provided that a side-chain amino group is properly positioned on the polypeptide donor [5]. Such a reactive group - usually belonging to a Lys residue (so-called ε) - needs to be located close to the N-terminus of the substrate to properly attain the active site base. In this study, we show that Lys-myristoylation makes deprotonation extremely difficult because of the salt bridge between the ammonium ion and the carboxylate base; in contrast, catalysis may proceed efficiently with the deprotonated ε–amino group. The deprotonated form of a Lys side chain is, however, extremely poorly abundant at physiological pH. This explains the low efficiency of the Lys-myristoylation reaction compared with Gly-myristoylation. This effect is therefore linked to the combined effect of the higher pK value of a side chain with respect to the α-amino group and the direct salt bridge. A major consequence is the higher affinity of the complex and further significant slowing of the catalytic rate. Primary amines appear to promote the strongest salt bridges over secondary or tertiary amines [56]. As the N-O distance needs to be less than 4 Å with an optimum in the 2.5-3.2 Å range and the angle made between the two bonds is best if around 0° [56], strengthening and optimizing binding requires a perfect fit in the active site crevice. This is ensured here by the linker with the more remote interaction areas. Salt bridges contribute only rarely to protein-ligand atomic interactions, far less than hydrophobic, hydrogen, or π-staking

[57]. Similar to NMT inhibitors, other systems have nevertheless demonstrated a major role for salt bridges in enzyme inhibition; due to their strength, they can induce a three orders of magnitude increase in potency, as in the case of protein kinase inhibitors [58]. This increase is comparable to the binding constant increase that the amino group of IMP-72 brings to IMP-358 when ligated to generate IMP-917, a compound closely related to IMP-1088 [18].

Conclusions

Here we show that peptide substrates displaying optimal fit and affinity with NMTs behave as inhibitors due to the persistent and slow dissociation time of the associated myristoylated product. Note that product release corresponds to the limiting step of NMT-catalyzed myristoylation [7]. The combination of these two inhibitory effects – one taking advantage of salt bridge formation and the other the slow dissociation of the product - led to the design of potent Lys-myristoylation-inspired inhibitors. These molecules represent a departure from classic substrates and can be considered first-in-class. By contrast, Gly-myristoylation peptides of the same series closely mimic the actual NMT substrate and already behave as potent inhibitors with binding constants in the nanomolar range. By using them to probe other NMTs and challenge their respective peptide-binding pockets, we reveal that NMTs of various phyla share common inhibitory properties with this series. Finally, we show that NMT-catalyzed myristoylation likely evolved and converged independently from two types of ligands, including those containing Asn3 and those with Ser6Lys7. Combining both features reduces catalytic turnover, as demonstrated by the strong inhibitory behavior of the reference peptide. This might explain why the reference sequence is not the favorable, unique myristoylation signal in any organism. A remarkable behavior is that of the Lys3-containing substrates, which can only tolerate Ser6Lys7 to promote Gly-myristoylation [5]. Taken together, the binding effects

of all positions are additive and together lead to potent inhibition. To ensure efficient protein myristoylation, recognition patterns on the substrates therefore require a trade-off between specific binding/targeting and an affinity that allows significant release of the product.

Acknowledgments

This work was supported by French National Research Agency (ANR) PalMyProt and DynaMYT (references n° ANR-2010-BLAN-1611-01; ANR-20-CE44-0013) and Fondation ARC (reference n° ARCPJA32020060002137) grants to TM. This work has benefited from a French State grant (Saclay Plant Sciences, reference n° ANR-17-EURE-0007, EUR SPS-GSR) under a France 2030 program (reference n° ANR-11-IDEX-0003), from the I2BC crystallization platform supported by FRISBI ANR-10-INSB-0005, from the facilities and expertise of the I2BC proteomic platform (Proteomic-Gif, SICaPS) supported by IBiSA, Ile de France Region, Plan Cancer, CNRS and Paris-Saclay University, and from COST Action CA20113, supported by COST (European Cooperation in Science and Technology). FR was supported by the PhD fellowship ARDoc program from Region Ile-de-France (17012695) and by Fondation pour la Recherche Médicale (FDT202001010779). We thank the French National Synchrotron Facility (SOLEIL) for provision of synchrotron radiation facilities and the staff of the PROXIMA-1/2 beamlines and the European Synchrotron Radiation Facility (ESRF) for help with data collection. We strongly acknowledge Benoît Castrec, Sarah Ciccone, Michel Desmadril, Magali Nicaise-Aumont, Jean-Pierre Le Caer, and Laila Sago for contributions in the early stages of the project.

Author contributions

Conceptualization, T.M.; Methodology, F.R., C.D. and T.M.; Investigation, F.R., C.D., R.F.D. and P.M.; Writing – Original Draft, C.G. and T.M.; Writing – Review & Editing, T.M.; Funding Acquisition, C.G. and T.M.; Resources, F.R., C.D., R.F.D., P.M. and T.M.; Supervision, T.M.

Declaration of interests

The authors declare no competing interests.

Supplemental information

Supplementary information is available for this paper.

Document S1. PDF file containing Figures S1-9 and Tables S1-3

Figure legends

Figure 1. Structure-activity relationship and associated inhibitory potency of the reference peptide series.

Error bars correspond to standard deviations of three replicates. (**a**) Impact of peptide length using the reference peptide series. The associated k_{cat}/K_m was measured and values highlighted and linked with a dotted line. When the value was less than 0.01 $M^{-1}.s^{-1}$ (i.e., the lowest detectable value), the IC_{50} was measured. The associated IC_{50} is indicated with plain bars with the scale indicated on the right ordinate scale. The scale is discontinuous starting from 10 µM and indicates a highest value of 100 µM. Inhibition properties were classified from the strongest (green) to intermediate (beige) to the weakest (red). (**b**) Apparent dissociation constants of some variants of the reference peptide series as measured in their presence with the kinetic assay. Values were calculated as reported in STAR Methods. (**c**) Binding constants of the same series as measured by ITC. (**d**) Structure-activity relationship analysis of the reference peptide series (G_2NCFSKPR) with unique substitutions indicated below were measured and reported. No bar indicates that the peptide is not a substrate within a value less than 0.01 $M^{-1}.s^{-1}$.

Figure 2. Cartoons detailing peptide binding within the active site groove of HsNMT1.

Magnified view of the active site of HsNMT1 crystallized in the presence of the indicated peptide and Myr-CoA. The peptide is shown in yellow (panels a-d), turquoise (panel e), or magenta (panel f); the myristate in purple; and the HsNMT1 surface around the ligand in grey (surface) and green (ribbon). Slice depth in panels a-d was 8-12 Å. The various pockets and

residues are displayed and hydrogen bonds are indicated as dashed lines. (**a-c**) GNCFSKPR (reference peptide). (**d**) GNLLSKFR (NPAP1). (**e**) GNCFSKPR-NH_2 (C-amidated variant of the reference peptide). The new hydrogen bonding around Arg9 is displayed. (**f**) GNCFSKPRVPTLK (reference peptide fused to mouse Bax-inhibiting tetrapeptide [59]). A close-up focusing on the C-terminal side of the peptide is displayed, and the residues are labelled in turquoise.

Figure 3. Binding modes of various peptides next to the catalytic base, the catalyst platform, and the aa2 pocket.

Pocket 3 - the pocket usually hosting amino acid 2 in Gly-myristoylation [1] - filling by the peptide moiety is schematized from the crystal structure data in the presence of various inhibitors or substrates. Gln496 bears the carboxy-terminal catalytic base. Hydrogen bonding is displayed as dashed lines. When water-mediated bonding occurs, the water molecule is displayed in turquoise (Wat2; see nomenclature of water molecules in Ref. [1]). Pocket 3 is displayed as a red cavity. Thr282 is the catalyst platform. Hydrogen bonding is displayed with a red dotted line. Distances in angstroms (Å) are indicated in red or in turquoise if water-mediated. Chirality of the peptide bonds is highlighted to show the high resemblance of Gly-Asn with *ac*[D-Orn]. (**a**) GNCSFSKRRA derivative of the reference peptide (PDB ID 6QRM). (**b**) Ac-KSFSKPR variant (*ac*K, PDB ID 7OWO, [5]). (**c**) a*c*[D-Orn] derivative of the reference peptide (PDB ID 8Q23). (**d**) Ala2-Lys3 derivative of the reference peptide (PDB ID 7OWN, [5]).

Figure 4. Characterization of Lys-myristoylation-inspired inhibitors of NMT.

The peptides are derived from the GK peptide. Error bars correspond to standard deviations of three replicates. (**a**) Apparent binding constants were derived from IC_{50} values according to [60]. All reactants but the reactive peptide SOS3 were pre-incubated in the presence of the two peptides for 30 minutes. The reaction was triggered by the addition of SOS3 and followed for 60 minutes. (**b**) Summary of the rules leading to NMT inhibition. (**c**) Plot showing that the *ac*[D-Orn] (black circles) and *ac*[D-Dab] (grey squares) derivatives display low partition ratios. The *ac*[L-Orn] inhibition pattern is indicated (black triangles). The reaction was triggered by the addition of the productive substrate after pre-incubation of the inhibitor for 60 minutes in the presence of Myr-CoA and HsNMT1. Time-course analysis was next performed to determine the remaining enzyme activity. A value of 100 was given to the value obtained in the absence of inhibitor due to the bi:bi mechanism, with Myr-CoA required to form the complex [27,61]. (**d**) 3D and (**e**) planar representations of the interaction networks around the *ac*[D-Orn] derivative bound to HsNMT1. (**f**) and (**g**) same as panels d and e, respectively, but with Dab. Distances in angstroms (Å) are indicated in red and displayed as red dotted lines.

Figure 5. Unlike Gly-myristoylation substrates, Lys-myristoylation substrates show tight pH sensitivity.

k_{cat}/K_m measurements of various HsNMT1 substrates (left bar ordinate) as a function of pH. The averaged value trend are shown as colored lines (green, panel a; orange, panel b). The percentage of the protonated form (right bar ordinate) is indicated with dashed black lines taking the values of 7.7 and 10.5 as the pK values of the alpha and epsilon groups of Gly and Lys residues, respectively. Complete pH range theoretical values are available in **Fig. S8b,c**. Error bars correspond to standard deviations of three replicates. (**a**) Gly-myristoylation substrates. K_m and k_{cat} profiles are provided in **Fig. S7** (**b**) Lys-myristoylation substrates. The

data associated with alanine-starting derivatives – also Lys-myristoylated - are provided in **Fig. S8a**. The same trend was observed.

Figure 6. Gly- and Lys-myristoylation display distinct inhibition mechanisms, both eventually leading to the same inhibitory complex.

(**a**) Inhibition model for the Gly-myristoylation-inspired series (G-Inhib). (**b**) Inhibition model for the Lys-myristoylation-inspired series (K-Inhib). KH^+-Inhib refers to the protonated amino group of the Lys side chain (Cε position), or any Lys mimic including Orn or D-Orn (Cδ position), while K-Inhib corresponds to the deprotonated form.

Figure 7. The reference inhibitor series displays close similarities to other potent inhibitors and is a potent inhibitor of representative members of NMT diversity.

(**a**) The 3D structures of HsNMT1 co-crystallized with the reference peptide (PDB Id 6QRM, grey, bottom) and Ac[D-Orn] inhibitor (PDB Id 8Q23, this study, orange, top), ScNMT with SC-58272 (PDB Id 2NMT, green), and HsNMT1 with DDD85646 (PDB Id 3IWE, turquoise) were aligned with that of HsNMT1 with IMP-1088 (PDB Id 5MU6, magenta). The NMT structures are not shown, and only the small inhibitor compounds are displayed as sticks with carbon in the above colors for each compound. Both top and bottom panels are in the same orientation, with the bottom panel slightly rotated around the y axis to better evidence the unique N-terminal residue of Gly2. Top, overlay of Ac[D-Orn] with SC-5872, IMP-1088, and DDD85646. Bottom, same as top but reference peptide used instead of Ac[D-Orn]. (**b**) IC_{50} values were measured in the presence of 50 µM of SOS3 peptide with increasing concentrations of the reference peptide in the presence of Myr-CoA and the indicated NMT. ScNMT was 0.1 µM; PfNMT, HsNMT1, HsNMT2, and AtNMT were all 0.5 µM. The $IC_{50}/[E_0]$ ratio is

calculated for each NMT. This ratio is a value that allows direct comparison of the respective binding constants. Error bars correspond to standard deviations of three replicates.

Tables

Table 1. Substitutions around the N-terminus of peptides promoting side chain MYR or NMT inhibition

Series	Peptide sequence	Short name (text & figures)	PDB ID	Kinetic parameters		
				k_{cat} (s^{-1})	K_m (µM)	k_{cat}/K_m ($s^{-1}.M^{-1}$)
acGK	ac-GKSFSKPR	*ac*GK	6KS2	0.0017 ± 0.0002	58 ± 15	30 ± 6
	ac-G[Orn]SFSKPR	*ac*G[Orn]	7OWP	0.0006 ± 0.0001	22 ± 3	29 ± 3
	ac-G[Dab]SFSKPR	*ac*G[Dab]		NM	NM	<<0.01
	ac-G[D-Orn]SFSKPR	*ac*G[D-Orn]		NM	NM	<<0.01
XK	AKSFSKPR	AK	7OWO	0.0006 ± 0.0002	14 ± 5	40 ± 11
	A[Orn]SFSKPR	A[Orn][c]		NM	NM	<<0.01
	A[D-Orn]SFSKPR	A[D-Orn][c]		NM	NM	<<0.01
	G[D-ORN]SFSKPR	G[D-Orn]		NM	NM	<<0.01
acK	ac-KSFSKPR	*ac*K	7OWO	0.0009 ± 0.0001	24 ± 10	37 ± 13
	ac-[Orn]SFSKPR	*ac*[Orn]		NM	NM	<<0.01
	ac-[D-Orn]SFSKPR	*ac*[D-Orn]	8Q23	NM	NM	<<0.01
	ac-[D-Dab]SFSKPR	*ac*[D-Dab]		NM	NM	<<0.01
	ac-[Dap]SFSKPR	*ac*[Dap]		NM	NM	<<0.01
	ac-[D-Orn]SNSKLK					1.5
K	KSFSKPR	K		0.00043 ± 0.00004	16 ± 6	27 ± 6
	[Orn]SFSKPR	[Orn]		>0.0002		2
	[D-Orn]SFSKPR	[D-Orn]		NM	NM	<<0.01
	[Dab]SFSKPR	[Dab][c]	8Q24	NM	NM	<<0.01

NM, not measurable; -, not measured or obtained.

STAR Methods

Resource availability

Further information and requests for resources and reagents should be directed to and will be fulfilled by the lead contact, Thierry Meinnel (thierry.meinnel@i2bc.paris-saclay.fr).

The crystal structures of NMT in complex with Myr-CoA and the peptides reported here have been deposited at the PDB under codes 8Q26, 8Q3T, 8Q3D, 8Q2Z, 8Q3S, 8Q23 and 8Q24.

Chemicals

All peptides (>95% purity) were purchased from Genscript Biotech Corporation (Rijswijk, Netherlands). NAD was purchased from Roche (Basel, Switzerland). All other chemicals were purchased from Sigma-Aldrich (St. Quentin, France). Stock solutions of myristoyl-CoA (0.2 mM) were prepared in sodium acetate, pH 5.6, and 1% Triton X-100, except for MALDI analysis, where cholate was used to reduce background.

As the N-terminal myristoylated residue is usually the second in the original ORF after the initial Met, we name this extreme N-terminal residue aa2 throughout this work.

NMT production

The long HsNMT1, HsNMT1[*l*], corresponding to residues 99-496 and devoid of the N-terminal unfolded domain, was cloned into a pET28 derivative vector featuring an N-terminal 10xHis tag fused with a Tobacco etch virus (TEV) protease cleavage site [62]. HsNMT1[*l*] was expressed at 22°C in BL21-PLysS Rosetta2 cells (Novagen, Sigma-Aldrich). Full-length HsNMT2, AtNMT, PfNMT, and ScNMT were purified as previously described [30,41]. HsNMT1[*l*] was purified with the His-Tag removed after TEV cleavage as previously described [6,62]. NMT overproducing cells are harvested by centrifugation and lysed by sonication after resuspension in 20 mM Tris–HCl (pH 8.0), 0.5 M NaCl, 5 mM 2-

mercaptoethanol, and 5 mM imidazole (buffer C) supplemented with 1 mg/mL lysozyme and 5 µL benzonase. After centrifugation, the clarified lysate is loaded at 3 mL/min onto a nickel affinity chromatography column (HisTrap Crude FF, 5 mL, GE Healthcare) and washed with buffer C with 25 mM imidazole. Elution is carried out at 2 mL/min with buffer C plus 0.25 M imidazole. The pool of purified HsNMT1 is next dialyzed overnight against 20 mM Tris-HCl (pH 8.9), 150 mM NaCl, 25 mM imidazole, and 5 mM 2-mercaptoethanol in the presence of TEV protease (1 mg per 15 mg purified protein). His-tag-free HsNMT1 is purified with a HisTrap Crude FF column. The flow-through with HsNMT1 is diluted five times in 20 mM Tris-HCl (pH 8.9) and 1 mM DTT (buffer B) and applied to an anion exchange chromatography column (HiTrap Q FF, 5 mL, GE Healthcare). HsNMT1 is eluted with buffer B supplemented with 0.2 M NaCl. Highly purified fractions are pooled, concentrated to 15–30 mg/ mL with an Amicon centrifugal filtration device (Merck Millipore) in 20 mM Tris–HCl (pH 8.0), 0.2 M NaCl, 1 mM DTT, and stored at -80°C before crystallization trials. Protein samples for kinetic analysis are stored at -20°C in the same buffer plus 55% glycerol.

Protein crystallization and structure determination

HsNMT1:Myr-CoA:inhibitor structures. The HsNMT1[*l*] crystal structure in complex with Myr-CoA was used to solve the structures of the complexes with ten different peptides in this study. Suitable crystals of HsNMT1:Myr-CoA:inhibitor complexes were obtained by co-crystallization using the hanging-drop vapor diffusion method at 20°C. Crystallization droplets were formed by mixing 2 µL of the HsNMT1:Myr-CoA:peptide complex (molar ratio 1:1.5:1.5) at 6-9 mg/mL with 2 µL of the precipitant solution containing 0.1 M $MgCl_2$, 0.2 M NaCl, 0.1 M sodium citrate pH 5.6, and 18-24% (w/v) PEG 6K or 8K. Crystals were cryoprotected in the reservoir solution supplemented with 15% (v/v) glycerol and flash cooled in liquid nitrogen. Complete X-ray datasets of HsNMT1:Myr-CoA:inhibitors were collected at

100*K* the French National Synchrotron Facility (SOLEIL) PROXIMA-1 or PROXIMA-2 beamlines or at the European Radiation Synchrotron Facility (ESRF) with the BM14, ID30A1/MASSIF1, and ID30A3/MASSIF3 beamlines.

Datasets were integrated with XDS [63] and scaled and reduced using AIMLESS from the CCP4 package [64]. Crystals belonged to the space group $P2_12_12$ with similar unit cell parameters (summarized in **Table S2**) and contained two NMT molecules per asymmetric unit. The structures of the HsNMT1:Myr-CoA:inhibitor complexes were solved using MOLREP [65]. C_α protein coordinates of the HsNMT1[*I*] model (PDB entry 5O9V) were used as the search model. Structures were subjected to alternating refinement cycles using REFMAC-5 and PHENIX and manual model building using COOT [66-68]. The good quality electron density maps also enabled refinement of substrate peptide, reaction intermediate, and reaction product molecules bound to HsNMT1 in each complex. Chemical compound libraries were generated using PRODRG server [69] in combination with eLBOW from the PHENIX suite. Difference electron density maps were calculated in PHENIX. Final model geometry was validated using MolProbity [70]. X-ray data collection and refinement statistics are summarized in **Table S2**. Figures were generated using PyMOL (DeLano Scientific LLC, http://pymol.sourceforge.net/). Omit electron density maps were calculated using PolderMap [71] from the PHENIX suite after omitting the peptide of each active site and excluding the bulk solvent around the omitted region. Ligand-protein interaction diagrams were generated with LigPlot+ v2.2.8 [72] and displayed in **Fig. S3**. A summary of the main features and figures related to the crystal structures associated to this work is provided in **Table S3**.

Measurements of activity and inhibition parameters

HsNMT1 activity was assayed at 30°C in a coupled assay using an updated, step-by-step, detailed version of the previously described protocol [73,74]. In brief, the reaction mixture

contained 50 mM Tris-HCl (pH 8.0), 1 mM $MgCl_2$, 0.193 mM EGTA, 0.32 mM DTT, 0.2 mM thiamine pyrophosphate, 2 mM pyruvate, 0.1 mg/mL of BSA, 0.1% Triton X-100, 2.5 mM NAD^+, 0.125 units/mL of porcine heart PDH (0.33 units/mg), 40 µM Myr-CoA, and 1-2000 µM peptides. Unless otherwise stated for tight binding studies, the reaction mixture was pre-incubated for 3 min at 30°C before starting the reaction by adding Myr-CoA. The final volume was 200 µL, and kinetics were followed by either fluorescence- or absorption-based spectrometry [74]. An Infinite M Nano$^+$ plate reader equipped with micro-injectors (Tecan, Lyon, France) was set at 340 nm to monitor the absorbance over time at 30°C. Briefly, a reaction mixture containing HsNMT1[*l*] at different concentrations of peptide acceptors was pre-incubated for 3 min at 30°C before starting the reaction with Myr-CoA. Myristoylation kinetics were monitored continuously for 30 min, and the data were fitted to obtain the initial velocities associated with each peptide concentration. Curve fits to obtain kinetic parameters were achieved by non-linear regression with GraphPad Prism 9.5 (GraphPad Software, La Jolla, CA). Parameters with standard errors were computed for all parameters using the complete dataset including replicates. Both k_{cat} and K_m kinetic parameters and associated standard deviations were obtained by fitting to the Michaelis–Menten equation [74]. k_{cat}/K_m values were derived from both parameters and the associated standard errors were calculated as described [74].

For inhibition assays, we used the same reaction mixture for up to 30 min at 30°C incubation in the presence of the inhibitor peptide and Myr-CoA. The reaction was triggered by the addition of G_2CSVSVKKK (SOS3) peptide and monitored for 30 min. Inhibition curves and associated IC_{50} values were fitted using the GraphPad absolute IC_{50} module with baseline set at 0. Inhibition constants were calculated as described in [36,60,75] with K_I = (IC_{50}-

[E]/2)/(1+[S]/K_m). The HsNMT1 concentration was 0.25 µM, and the substrate (G_2CSVSKKK; K_m=18±3 µM [41,73]) was used at a concentration of 20 µM.

Microcalorimetry

Purified HsNMT1 was dissolved in 20 mM H_3PO_4 pH 7.4, 0.3 M NaCl buffer. The binding parameters of HsNMT1 inhibitors were monitored at 30°C by isothermal titration calorimetry (ITC) on an ITC200 microcalorimeter (MicroCal, Malvern Panalytical, Malvern, UK). Peptides were dissolved in the same buffer. A total of 20-25 injections of 1.5-2 µL peptide (250-350 µM) were made from a computer-controlled 40 µL microsyringe at 180-240 s intervals into the solution (30 µM HsNMT1 mixed or not with 30 µM Myr-CoA, volume cell = 0.2 mL), with stirring at 310 rpm. Experimental data were fit to a theoretical titration curve using Origin software with ΔH (the enthalpy change), K_a (the association binding constant in M^{-1}), and n (the number of binding sites per monomer) as adjustable parameters and the total protein concentration and the free and total ligand concentrations as known parameters. Examples of analysis for each reported measurement are given in **Fig. S3a-m**.

Mass spectrometry

For MALDI-ToF/ToF analysis, 300 µL of a mixture containing 50 mM Tris (pH 8), 0.193 mM EGTA, 1 mM $MgCl_2$, 1 mM DTT, 5 µM sodium cholate, 0.04 mM Myr-CoA solution (stock solution 0.2 mM Myr-CoA, 10 mM sodium acetate, 2.5 µM sodium cholate), 0.5 µM NMT, and 100 µM of synthetic peptide were incubated at 30°C. The myristoylation reaction was followed over time by collecting 10 µL samples further diluted in 90 µL of water/acetonitrile solution. The different samples were then diluted five times in the matrix solution made of 5 mg/mL of α-cyano-4-hydroxycinnamic acid solubilized in water/formic acid/acetonitrile (50/50/0.1%). 1 µL of each dilution was spotted on a metal target and dried. MS and MS/MS

spectra of each sample were acquired and analyzed with an AB SCIEX 5800 instrument in positive ion mode as reported in [5].

References

1. Meinnel, T., Dian, C., and Giglione, C. (2020). Myristoylation, an ancient protein modification mirroring eukaryogenesis and evolution. Trends Biochem Sci *45*, 619-632. 10.1016/j.tibs.2020.03.007.
2. Giglione, C., and Meinnel, T. (2022). Mapping the myristoylome through a complete understanding of protein myristoylation biochemistry. Prog Lipid Res *85*, 101139. 10.1016/j.plipres.2021.101139.
3. Kosciuk, T., and Lin, H. (2020). N-Myristoyltransferase as a glycine and lysine myristoyltransferase in cancer, immunity, and infections. ACS Chem Biol *15*, 1747-1758. 10.1021/acschembio.0c00314.
4. Kosciuk, T., Price, I.R., Zhang, X., Zhu, C., Johnson, K.N., Zhang, S., Halaby, S.L., Komaniecki, G.P., Yang, M., DeHart, C.J., et al. (2020). NMT1 and NMT2 are lysine myristoyltransferases regulating the ARF6 GTPase cycle. Nat Commun *11*, 1067. 10.1038/s41467-020-14893-x.
5. Rivière, F., Dian, C., Dutheil, R.F., Monassa, P., Giglione, C., and Meinnel, T. (2022). Structural and large-scale analysis unveil the intertwined paths promoting NMT-catalyzed lysine and glycine myristoylation. J Mol Biol *434*, 167843. 10.1016/j.jmb.2022.167843.
6. Dian, C., Pérez-Dorado, I., Rivière, F., Asensio, T., Legrand, P., Ritzefeld, M., Shen, M., Cota, E., Meinnel, T., Tate, E.W., and Giglione, C. (2020). High-resolution snapshots of human N-myristoyltransferase in action illuminate a mechanism promoting N-terminal Lys and Gly myristoylation. Nat Commun *11*, 1132. 10.1038/s41467-020-14847-3.
7. Meinnel, T. (2022). Comment on "Binding affinity determines substrate specificity and enables discovery of substrates for N-Myristoyltransferases". ACS Catal *12*, 8195-8201. 10.1021/acscatal.2c01060.
8. Bhatnagar, R.S., Jackson-Machelski, E., McWherter, C.A., and Gordon, J.I. (1994). Isothermal titration calorimetric studies of Saccharomyces cerevisiae myristoyl-

CoA:protein N-myristoyltransferase. Determinants of binding energy and catalytic discrimination among acyl-CoA and peptide ligands. J Biol Chem *269*, 11045-11053.

9. Rudnick, D.A., McWherter, C.A., Rocque, W.J., Lennon, P.J., Getman, D.P., and Gordon, J.I. (1991). Kinetic and structural evidence for a sequential ordered Bi Bi mechanism of catalysis by Saccharomyces cerevisiae myristoyl-CoA:protein N-myristoyltransferase. J Biol Chem *266*, 9732-9739. 10.1016/S0021-9258(18)92882-6.
10. Towler, D.A., Adams, S.P., Eubanks, S.R., Towery, D.S., Jackson-Machelski, E., Glaser, L., and Gordon, J.I. (1987). Purification and characterization of yeast myristoyl CoA:protein N-myristoyltransferase. Proc Natl Acad Sci U S A *84*, 2708-2712. 10.1073/pnas.84.9.2708.
11. Wright, M.H., Clough, B., Rackham, M.D., Rangachari, K., Brannigan, J.A., Grainger, M., Moss, D.K., Bottrill, A.R., Heal, W.P., Broncel, M., et al. (2014). Validation of N-myristoyltransferase as an antimalarial drug target using an integrated chemical biology approach. Nat Chem *6*, 112-121. 10.1038/nchem.1830.
12. Thinon, E., Serwa, R.A., Broncel, M., Brannigan, J.A., Brassat, U., Wright, M.H., Heal, W.P., Wilkinson, A.J., Mann, D.J., and Tate, E.W. (2014). Global profiling of co- and post-translationally N-myristoylated proteomes in human cells. Nat Commun *5*, 4919. 10.1038/ncomms5919.
13. Broncel, M., Serwa, R.A., Ciepla, P., Krause, E., Dallman, M.J., Magee, A.I., and Tate, E.W. (2015). Multifunctional reagents for quantitative proteome-wide analysis of protein modification in human cells and dynamic profiling of protein lipidation during vertebrate development. Angew Chem Int Ed Engl *54*, 5948-5951. 10.1002/anie.201500342.
14. Wright, M.H., Paape, D., Price, H.P., Smith, D.F., and Tate, E.W. (2016). Global profiling and inhibition of protein lipidation in vector and host stages of the sleeping sickness parasite Trypanosoma brucei. ACS Infect Dis *2*, 427-441. 10.1021/acsinfecdis.6b00034.
15. Broncel, M., Dominicus, C., Vigetti, L., Nofal, S.D., Bartlett, E.J., Touquet, B., Hunt, A., Wallbank, B.A., Federico, S., Matthews, S., et al. (2020). Profiling of myristoylation in Toxoplasma gondii reveals an N-myristoylated protein important for host cell penetration. eLife *9*, e57861. 10.7554/eLife.57861.

16. Majeran, W., Le Caer, J.P., Ponnala, L., Meinnel, T., and Giglione, C. (2018). Targeted profiling of A. thaliana sub-proteomes illuminates new co- and post-translationally N-terminal myristoylated proteins. Plant Cell *30*, 543-562. 10.1105/tpc.17.00523.

17. Maurer-Stroh, S., and Eisenhaber, F. (2004). Myristoylation of viral and bacterial proteins. Trends Microbiol *12*, 178-185. 10.1016/j.tim.2004.02.006.

18. Mousnier, A., Bell, A.S., Swieboda, D.P., Morales-Sanfrutos, J., Perez-Dorado, I., Brannigan, J.A., Newman, J., Ritzefeld, M., Hutton, J.A., Guedan, A., et al. (2018). Fragment-derived inhibitors of human N-myristoyltransferase block capsid assembly and replication of the common cold virus. Nat Chem *10*, 599-606. 10.1038/s41557-018-0039-2.

19. Priyamvada, L., Kallemeijn, W.W., Faronato, M., Wilkins, K., Goldsmith, C.S., Cotter, C.A., Ojeda, S., Solari, R., Moss, B., Tate, E.W., and Satheshkumar, P.S. (2022). Inhibition of vaccinia virus L1 N-myristoylation by the host N-myristoyltransferase inhibitor IMP-1088 generates non-infectious virions defective in cell entry. PLoS Pathog *18*, e1010662. 10.1371/journal.ppat.1010662.

20. Saber, S.H., Ojha, R., Quirin, T., Strandin, T., Kant, R., Kareinen, L., Yak, N., Sironen, T., Vapalahti, O., Balistreri, G., and Joensuu, M. (2023). The infectivity of SARS-CoV-2 progeny virions requires the activity of host cell N-myristoyltransferases and it is severely compromised by their inhibition. bioRxiv, 2023.2003.2003.530798. 10.1101/2023.03.03.530798.

21. Beauchamp, E., Yap, M.C., Iyer, A., Perinpanayagam, M.A., Gamma, J.M., Vincent, K.M., Lakshmanan, M., Raju, A., Tergaonkar, V., Tan, S.Y., et al. (2020). Targeting N-myristoylation for therapy of B-cell lymphomas. Nat Commun *11*, 5348. 10.1038/s41467-020-18998-1.

22. Tate, E.W., Soday, L., de la Lastra, A.L., Wang, M., and Lin, H. (2024). Protein lipidation in cancer: mechanisms, dysregulation and emerging drug targets. Nat Rev Cancer. 10.1038/s41568-024-00666-x.

23. Frearson, J.A., Brand, S., McElroy, S.P., Cleghorn, L.A., Smid, O., Stojanovski, L., Price, H.P., Guther, M.L., Torrie, L.S., Robinson, D.A., et al. (2010). N-myristoyltransferase inhibitors as new leads to treat sleeping sickness. Nature *464*, 728-732. 10.1038/nature08893.

24. Schlott, A.C., Knuepfer, E., Green, J.L., Hobson, P., Borg, A.J., Morales-Sanfrutos, J., Perrin, A.J., Maclachlan, C., Collinson, L.M., Snijders, A.P., et al. (2021). Inhibition of protein N-myristoylation blocks Plasmodium falciparum intraerythrocytic development, egress and invasion. PLoS Biol *19*, e3001408. 10.1371/journal.pbio.3001408.

25. Schlott, A.C., Mayclin, S., Reers, A.R., Coburn-Flynn, O., Bell, A.S., Green, J., Knuepfer, E., Charter, D., Bonnert, R., Campo, B., et al. (2019). Structure-guided identification of resistance breaking antimalarial N-myristoyltransferase inhibitors. Cell Chem Biol *26*, 991-1000.e1007. 10.1016/j.chembiol.2019.03.015.

26. Rodríguez-Hernández, D., Vijayan, K., Zigweid, R., Fenwick, M.K., Sankaran, B., Roobsoong, W., Sattabongkot, J., Glennon, E.K.K., Myler, P.J., Sunnerhagen, P., et al. (2023). Identification of potent and selective N-myristoyltransferase inhibitors of Plasmodium vivax liver stage hypnozoites and schizonts. Nat Commun *14*, 5408. 10.1038/s41467-023-41119-7.

27. Bhatnagar, R.S., Ashrafi, K., Futterer, K., Waksman, G., and Gordon, J.I. (2001). Biology and enzymology of protein N-myristoylation. In The Enzymes, F. Tamanoi, and D.S. Sigman, eds. (Academic Press), pp. 241-286. 10.1016/S1874-6047(01)80022-6.

28. Fang, W., Robinson, D.A., Raimi, O.G., Blair, D.E., Harrison, J.R., Lockhart, D.E., Torrie, L.S., Ruda, G.F., Wyatt, P.G., Gilbert, I.H., and van Aalten, D.M. (2015). N-myristoyltransferase is a cell wall target in Aspergillus fumigatus. ACS Chem Biol *10*, 1425-1434. 10.1021/cb5008647.

29. Fenwick, M.K., Reers, A.R., Liu, Y., Zigweid, R., Sankaran, B., Shin, J., Hulverson, M.A., Hammerson, B., Fernández Álvaro, E., Myler, P.J., et al. (2023). Identification of and structural insights into hit compounds targeting N-myristoyltransferase for Cryptosporidium drug development. ACS Infect Dis. 10.1021/acsinfecdis.3c00151.

30. Castrec, B., Dian, C., Ciccone, S., Ebert, C.L., Bienvenut, W.V., Le Caer, J.-P., Steyaert, J.-M., Giglione, C., and Meinnel, T. (2018). Structural and genomic decoding of human and plant myristoylomes reveals a definitive recognition pattern. Nat Chem Biol *14*, 671-679. 10.1038/s41589-018-0077-5.

31. Takamitsu, E., Otsuka, M., Haebara, T., Yano, M., Matsuzaki, K., Kobuchi, H., Moriya, K., and Utsumi, T. (2015). Identification of human N-myristoylated proteins from

human complementary DNA resources by cell-free and cellular metabolic labeling analyses. PLoS One *10*, e0136360. 10.1371/journal.pone.0136360.

32. Traverso, J.A., Micalella, C., Martinez, A., Brown, S.C., Satiat-Jeunemaitre, B., Meinnel, T., and Giglione, C. (2013). Roles of N-Terminal fatty acid acylations in membrane compartment partitioning: Arabidopsis h-type thioredoxins as a case study. Plant Cell *25*, 1056-1077. 10.1105/tpc.112.106849.

33. Neumann, L.C., Feiner, N., Meyer, A., Buiting, K., and Horsthemke, B. (2014). The imprinted NPAP1 gene in the Prader-Willi syndrome region belongs to a POM121-related family of retrogenes. Genome Biol Evol *6*, 344-351. 10.1093/gbe/evu019.

34. Hougland, J.L., Hicks, K.A., Hartman, H.L., Kelly, R.A., Watt, T.J., and Fierke, C.A. (2010). Identification of novel peptide substrates for protein farnesyltransferase reveals two substrate classes with distinct sequence selectivities. J Mol Biol *395*, 176-190. 10.1016/j.jmb.2009.10.038.

35. Farazi, T.A., Manchester, J.K., and Gordon, J.I. (2000). Transient-state kinetic analysis of Saccharomyces cerevisiae myristoylCoA:protein N-myristoyltransferase reveals that a step after chemical transformation is rate limiting. Biochemistry *39*, 15807-15816. 10.1021/bi002074t.

36. Copeland, R.A. (2005). Evaluation of enzyme inhibitors in drug discovery: a guide for medicinal chemists and pharmacologists (John Wiley & Sons).

37. Salah Ud-Din, A.I., Tikhomirova, A., and Roujeinikova, A. (2016). Structure and functional diversity of GCN5-related N-acetyltransferases (GNAT). Int J Mol Sci *17*, E1018. 10.3390/ijms17071018.

38. Bhatnagar, R.S., Futterer, K., Farazi, T.A., Korolev, S., Murray, C.L., Jackson-Machelski, E., Gokel, G.W., Gordon, J.I., and Waksman, G. (1998). Structure of N-myristoyltransferase with bound myristoylCoA and peptide substrate analogs. Nat Struct Biol *5*, 1091-1097. 10.1038/4202.

39. Sangha, R., Davies, N.M., Namdar, A., Chu, M., Spratlin, J., Beauchamp, E., Berthiaume, L.G., and Mackey, J.R. (2022). Novel, first-in-human, oral PCLX-001 treatment in a patient with relapsed diffuse large B-cell lymphoma. Curr Oncol *29*, 1939-1946.

40. Mackey, J.R., Lai, J., Chauhan, U., Beauchamp, E., Dong, W.F., Glubrecht, D., Sim, Y.W., Ghosh, S., Bigras, G., Lai, R., and Berthiaume, L.G. (2021). N-

myristoyltransferase proteins in breast cancer: prognostic relevance and validation as a new drug target. Breast Cancer Res Treat *186*, 79-87. 10.1007/s10549-020-06037-y.

41. Traverso, J.A., Giglione, C., and Meinnel, T. (2013). High-throughput profiling of N-myristoylation substrate specificity across species including pathogens. Proteomics *13*, 25-36. 10.1002/pmic.201200375.

42. Nagarajan, S.R., Devadas, B., Zupec, M.E., Freeman, S.K., Brown, D.L., Lu, H.F., Mehta, P.P., Kishore, N.S., McWherter, C.A., Getman, D.P., et al. (1997). Conformationally constrained [p-(omega-aminoalkyl)phenacetyl]-L-seryl-L-lysyl dipeptide amides as potent peptidomimetic inhibitors of Candida albicans and human myristoyl-CoA:protein N-myristoyl transferase. J Med Chem *40*, 1422-1438. 10.1021/jm9608671.

43. McWherter, C.A., Rocque, W.J., Zupec, M.E., Freeman, S.K., Brown, D.L., Devadas, B., Getman, D.P., Sikorski, J.A., and Gordon, J.I. (1997). Scanning alanine mutagenesis and de-peptidization of a *Candida albicans* myristoyl-CoA:protein N-myristoyltransferase octapeptide substrate reveals three elements critical for molecular recognition. J Biol Chem *272*, 11874-11880. 10.1074/jbc.272.18.11874.

44. Devadas, B., Freeman, S.K., Zupec, M.E., Lu, H.F., Nagarajan, S.R., Kishore, N.S., Lodge, J.K., Kuneman, D.W., McWherter, C.A., Vinjamoori, D.V., et al. (1997). Design and synthesis of novel imidazole-substituted dipeptide amides as potent and selective inhibitors of Candida albicans myristoylCoA:protein N-myristoyltransferase and identification of related tripeptide inhibitors with mechanism-based antifungal activity. J Med Chem *40*, 2609-2625.

45. Devadas, B., Freeman, S.K., McWherter, C.A., Kishore, N.S., Lodge, J.K., Jackson-Machelski, E., Gordon, J.I., and Sikorski, J.A. (1998). Novel biologically active nonpeptidic inhibitors of myristoylCoA:protein N-myristoyltransferase. J Med Chem *41*, 996-1000. 10.1021/jm980001q.

46. Olaleye, T.O., Brannigan, J.A., Roberts, S.M., Leatherbarrow, R.J., Wilkinson, A.J., and Tate, E.W. (2014). Peptidomimetic inhibitors of N-myristoyltransferase from human malaria and leishmaniasis parasites. Org Biomol Chem *12*, 8132-8137. 10.1039/c4ob01669f.

47. Zhao, C., and Ma, S. (2014). Recent Advances in The Discovery of N-Myristoyltransferase Inhibitors. ChemMedChem *9*, 2425-2437. 10.1002/cmdc.201402174.

48. Bell, A.S., Mills, J.E., Williams, G.P., Brannigan, J.A., Wilkinson, A.J., Parkinson, T., Leatherbarrow, R.J., Tate, E.W., Holder, A.A., and Smith, D.F. (2012). Selective inhibitors of protozoan protein N-myristoyltransferases as starting points for tropical disease medicinal chemistry programs. PLoS Negl Trop Dis *6*, e1625. 10.1371/journal.pntd.0001625.

49. Paape, D., Bell, A.S., Heal, W.P., Hutton, J.A., Leatherbarrow, R.J., Tate, E.W., and Smith, D.F. (2014). Using a non-image-based medium-throughput assay for screening compounds targeting N-myristoylation in intracellular Leishmania amastigotes. PLoS Negl Trop Dis *8*, e3363. 10.1371/journal.pntd.0003363.

50. Goncalves, V., Brannigan, J.A., Whalley, D., Ansell, K.H., Saxty, B., Holder, A.A., Wilkinson, A.J., Tate, E.W., and Leatherbarrow, R.J. (2012). Discovery of Plasmodium vivax N-myristoyltransferase inhibitors: screening, synthesis, and structural characterization of their binding mode. J Med Chem *55*, 3578-3582. 10.1021/jm300040p.

51. Spassov, D.S., Atanasova, M., and Doytchinova, I. (2023). A role of salt bridges in mediating drug potency: A lesson from the N-myristoyltransferase inhibitors. Front Mol Biosci *9*, 1066029. 10.3389/fmolb.2022.1066029.

52. Devabhaktuni, A., Lin, S., Zhang, L., Swaminathan, K., Gonzalez, C.G., Olsson, N., Pearlman, S.M., Rawson, K., and Elias, J.E. (2019). TagGraph reveals vast protein modification landscapes from large tandem mass spectrometry datasets. Nat Biotechnol *37*, 469-479. 10.1038/s41587-019-0067-5.

53. Meinnel, T., and Giglione, C. (2022). N-terminal modifications, the associated processing machinery, and their evolution in plastid-containing organisms. J Exp Bot *73*, 6013-6033. 10.1093/jxb/erac290.

54. Rosen, C.B., and Francis, M.B. (2017). Targeting the N terminus for site-selective protein modification. Nat Chem Biol *13*, 697-705. 10.1038/nchembio.2416.

55. Pace, C.N., Grimsley, G.R., and Scholtz, J.M. (2009). Protein ionizable groups: pK values and their contribution to protein stability and solubility. J Biol Chem *284*, 13285-13289. 10.1074/jbc.R800080200.

56. Kurczab, R., Śliwa, P., Rataj, K., Kafel, R., and Bojarski, A.J. (2018). Salt Bridge in Ligand-Protein Complexes-Systematic Theoretical and Statistical Investigations. J Chem Inf Model *58*, 2224-2238. 10.1021/acs.jcim.8b00266.

57. Ferreira de Freitas, R., and Schapira, M. (2017). A systematic analysis of atomic protein-ligand interactions in the PDB. Medchemcomm *8*, 1970-1981. 10.1039/c7md00381a.

58. Peng, Y.H., Shiao, H.Y., Tu, C.H., Liu, P.M., Hsu, J.T., Amancha, P.K., Wu, J.S., Coumar, M.S., Chen, C.H., Wang, S.Y., et al. (2013). Protein kinase inhibitor design by targeting the Asp-Phe-Gly (DFG) motif: the role of the DFG motif in the design of epidermal growth factor receptor inhibitors. J Med Chem *56*, 3889-3903. 10.1021/jm400072p.

59. Gomez, J.A., Gama, V., Yoshida, T., Sun, W., Hayes, P., Leskov, K., Boothman, D., and Matsuyama, S. (2007). Bax-inhibiting peptides derived from Ku70 and cell-penetrating pentapeptides. Biochem Soc Trans *35*, 797-801. 10.1042/bst0350797.

60. Copeland, R.A., Lombardo, D., Giannaras, J., and Decicco, C.P. (1995). Estimating KI values for tight binding inhibitors from dose-response plots. Bioorg Med Chem Lett *5*, 1947-1952. 10.1016/0960-894X(95)00330-V.

61. Johnson, D.R., Bhatnagar, R.S., Knoll, L.J., and Gordon, J.I. (1994). Genetic and biochemical studies of protein N-myristoylation. Annu Rev Biochem *63*, 869-914. 10.1146/annurev.bi.63.070194.004253.

62. Monassa, P., Rivière, F., Dian, C., Frottin, F., Giglione, C., and Meinnel, T. (2023). Biochemical and structural analysis of N-myristoyltransferase mediated protein tagging. Methods Enzymol *684*, 135-166. 10.1016/bs.mie.2023.02.016.

63. Kabsch, W. (1993). Automatic processing of rotation diffraction data from crystals of initially unknown symmetry and cell constants. J Appl Crystallogr *26*, 795-800. 10.1107/S0021889893005588.

64. Evans, P.R., and Murshudov, G.N. (2013). How good are my data and what is the resolution? Acta Crystallogr D Biol Crystallogr *69*, 1204-1214. 10.1107/S0907444913000061.

65. Vagin, A., and Teplyakov, A. (1997). MOLREP: an automated program for molecular replacement. J. Appl. Cryst. *30*, 1022-1225. 10.1107/S0907444909042589.

66. Murshudov, G.N., Skubak, P., Lebedev, A.A., Pannu, N.S., Steiner, R.A., Nicholls, R.A., Winn, M.D., Long, F., and Vagin, A.A. (2011). REFMAC5 for the refinement of macromolecular crystal structures. Acta Crystallogr D Biol Crystallogr *67*, 355-367. 10.1107/S0907444911001314.

67. Adams, P.D., Afonine, P.V., Bunkoczi, G., Chen, V.B., Davis, I.W., Echols, N., Headd, J.J., Hung, L.W., Kapral, G.J., Grosse-Kunstleve, R.W., et al. (2010). PHENIX: a comprehensive Python-based system for macromolecular structure solution. Acta Crystallogr D Biol Crystallogr *66*, 213-221. 10.1107/S0907444909052925.

68. Emsley, P., Lohkamp, B., Scott, W.G., and Cowtan, K. (2010). Features and development of Coot. Acta Crystallogr D Biol Crystallogr *66*, 486-501. 10.1107/S0907444910007493.

69. Schuttelkopf, A.W., and van Aalten, D.M. (2004). PRODRG: a tool for high-throughput crystallography of protein-ligand complexes. Acta Crystallographica Section D *60*, 1355-1363. 10.1107/S0907444904011679.

70. Chen, V.B., Arendall, W.B., 3rd, Headd, J.J., Keedy, D.A., Immormino, R.M., Kapral, G.J., Murray, L.W., Richardson, J.S., and Richardson, D.C. (2010). MolProbity: all-atom structure validation for macromolecular crystallography. Acta Crystallogr D Biol Crystallogr *66*, 12-21. 10.1107/S0907444909042073.

71. Liebschner, D., Afonine, P.V., Moriarty, N.W., Poon, B.K., Sobolev, O.V., Terwilliger, T.C., and Adams, P.D. (2017). Polder maps: improving OMIT maps by excluding bulk solvent. Acta Crystallogr D Struct Biol *73*, 148-157. 10.1107/s2059798316018210.

72. Laskowski, R.A., and Swindells, M.B. (2011). LigPlot+: multiple ligand-protein interaction diagrams for drug discovery. J Chem Inf Model *51*, 2778-2786. 10.1021/ci200227u.

73. Boisson, B., and Meinnel, T. (2003). A continuous assay of myristoyl-CoA:protein N-myristoyltransferase for proteomic analysis. Anal Biochem *322*, 116-123. 10.1016/j.ab.2003.07.007.

74. Rivière, F., Monassa, P., Giglione, C., and Meinnel, T. (2023). Kinetic and catalytic features of N-myristoyltransferases. Methods Enzymol *684*, 167-190. 10.1016/bs.mie.2023.02.018.

75. Fieulaine, S., Boularot, A., Artaud, I., Desmadril, M., Dardel, F., Meinnel, T., and Giglione, C. (2011). Trapping conformational states along ligand-binding dynamics of

peptide deformylase: the impact of induced fit on enzyme catalysis. PLoS Biol *9*, e1001066. 10.1371/journal.pbio.1001066.

Figure 1

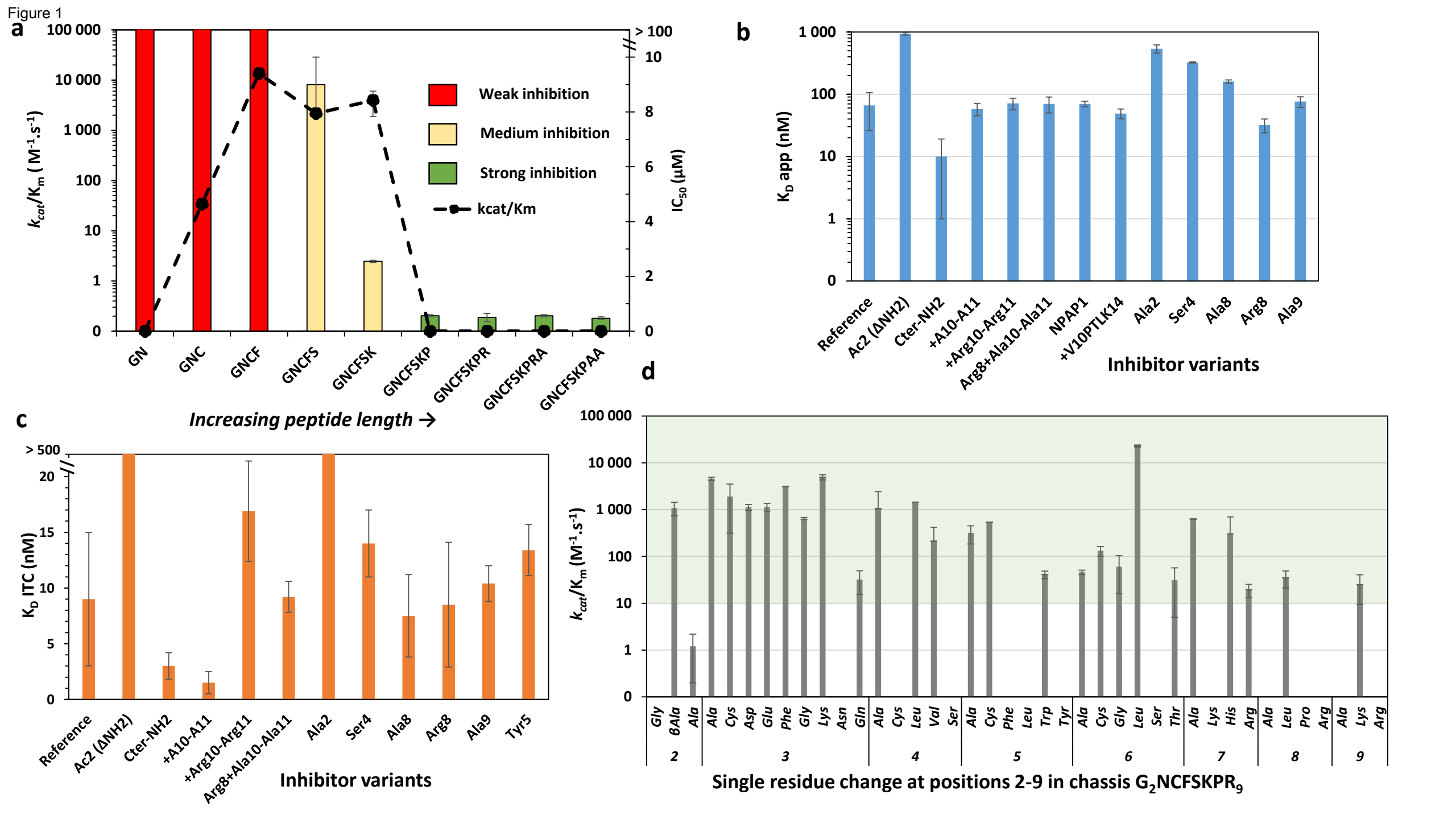
a
100 000
10 000
1 000
100
10
1
0
> 100
10
8
6
4
2
0
k_{cat}/K_m ($M^{-1}.s^{-1}$)
IC_{50} (µM)
Weak inhibition
Medium inhibition
Strong inhibition
kcat/Km
GN
GNC
GNCF
GNCFS
GNCFSK
GNCFSKP
GNCFSKPR
GNCFSKPRA
GNCFSKPAA
Increasing peptide length →
b
1 000
100
10
1
0
K_D app (nM)
Reference
Ac2 (ΔNH2)
Cter-NH2
+A10-A11
+Arg10-Arg11
Arg8+Ala10-Ala11
NPAP1
+V10PTLK14
Ala2
Ser4
Ala8
Arg8
Ala9
Inhibitor variants
c
> 500
20
15
10
5
0
K_D ITC (nM)
Reference
Ac2 (ΔNH2)
Cter-NH2
+A10-A11
+Arg10-Arg11
Arg8+Ala10-Ala11
Ala2
Ser4
Ala8
Arg8
Ala9
Tyr5
Inhibitor variants
d
100 000
10 000
1 000
100
10
1
0
k_{cat}/K_m ($M^{-1}.s^{-1}$)
Gly βAla Ala
Ala Cys Asp Glu Phe Gly Lys Asn Gln
Ala Cys Leu Val Ser
Ala Cys Phe Leu Trp Tyr
Ala Cys Gly Leu Ser Thr
Ala Lys His Arg
Ala Leu Pro Arg
Ala Lys Arg
2
3
4
5
6
7
8
9
Single residue change at positions 2-9 in chassis $G_2NCFSKPR_9$

Figure 2

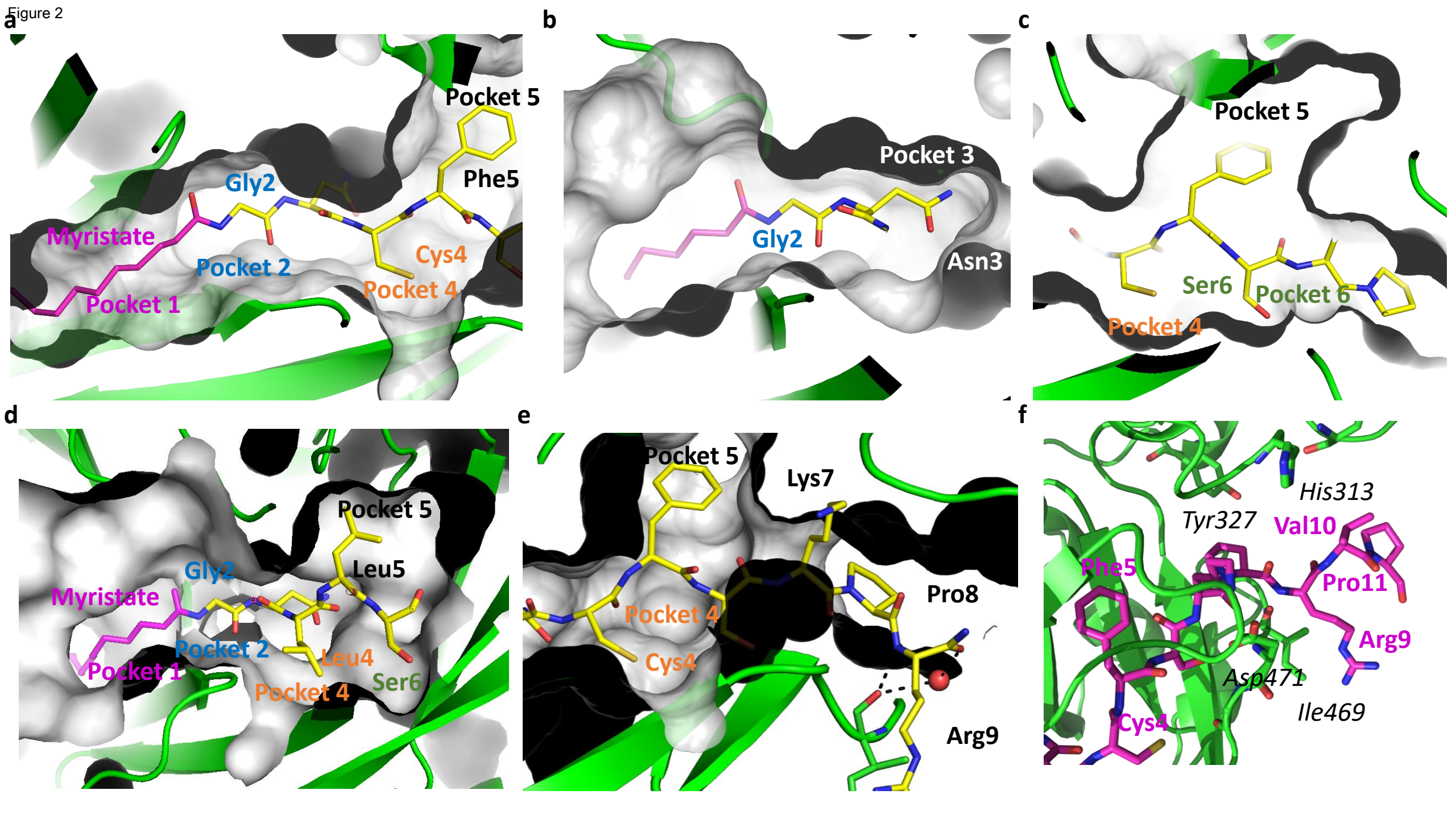
a
Pocket 5
Phe5
Gly2
Myristate
Pocket 2
Cys4
Pocket 4
Pocket 1
b
Pocket 3
Gly2
Asn3
c
Pocket 5
Ser6
Pocket 6
Pocket 4
d
Pocket 5
Gly2
Leu5
Myristate
Pocket 2
Leu4
Pocket 1
Pocket 4
Ser6
e
Pocket 5
Lys7
Pocket 4
Pro8
Cys4
Arg9
f
His313
Tyr327
Val10
Phe5
Pro11
Arg9
Asp471
Ile469
Cys4

Figure 3

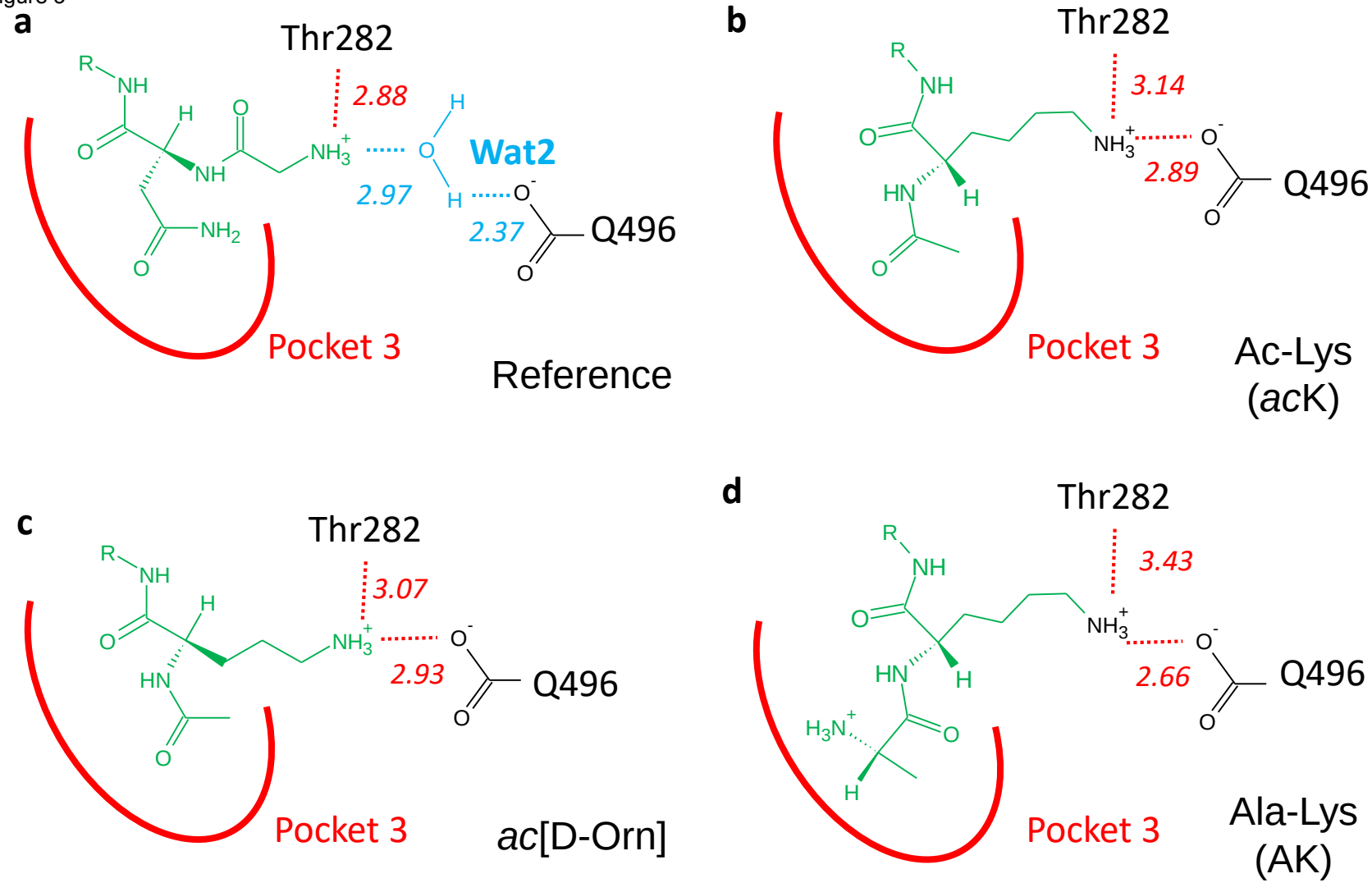
a
Thr282
2.88
Wat2
2.97
2.37
Q496
Pocket 3
Reference
b
Thr282
3.14
2.89
Q496
Pocket 3
Ac-Lys
(acK)
c
Thr282
3.07
2.93
Q496
Pocket 3
ac[D-Orn]
d
Thr282
3.43
2.66
Q496
Pocket 3
Ala-Lys
(AK)

Figure 4

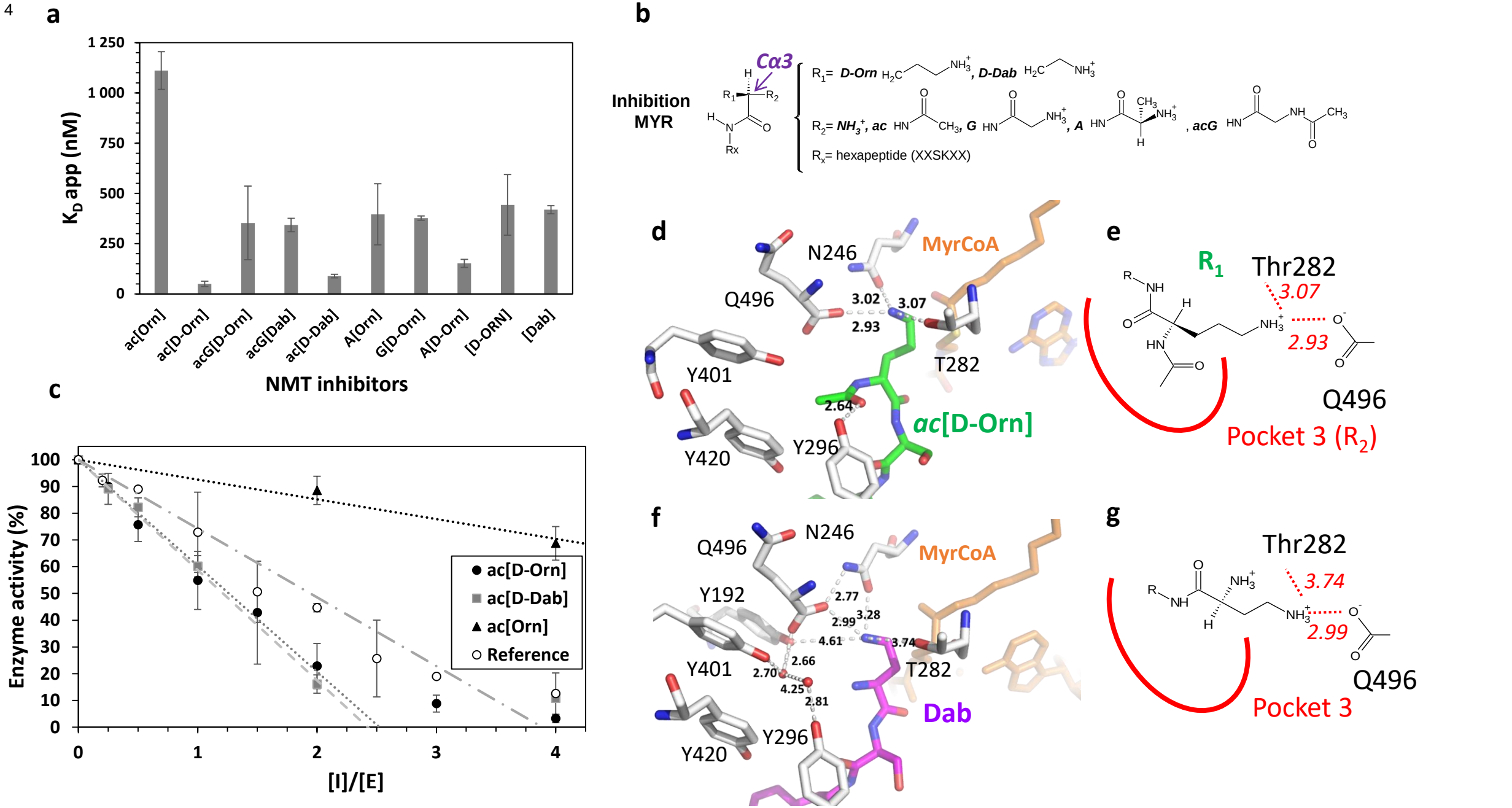
a
1 250
1 000
750
500
250
0
K_D app (nM)
ac[Orn]
ac[D-Orn]
acG[D-Orn]
acG[Dab]
ac[D-Dab]
A[Orn]
G[D-Orn]
A[D-Orn]
[D-ORN]
[Dab]
NMT inhibitors
b
Inhibition MYR
Cα3
R_1= D-Orn, D-Dab
R_2= NH_3^+, ac, G, A, acG
R_x= hexapeptide (XXSKXX)
c
100
90
80
70
60
50
40
30
20
10
0
Enzyme activity (%)
0
1
2
3
4
[I]/[E]
ac[D-Orn]
ac[D-Dab]
ac[Orn]
Reference
d
N246
MyrCoA
Q496
3.02
3.07
2.93
Y401
T282
2.64
ac[D-Orn]
Y296
Y420
e
R_1
Thr282
3.07
2.93
Q496
Pocket 3 (R_2)
f
Q496
N246
MyrCoA
Y192
2.77
2.99
3.28
4.61
3.74
2.66
2.70
4.25
2.81
Y401
T282
Dab
Y296
Y420
g
Thr282
3.74
2.99
Q496
Pocket 3

Figure 5

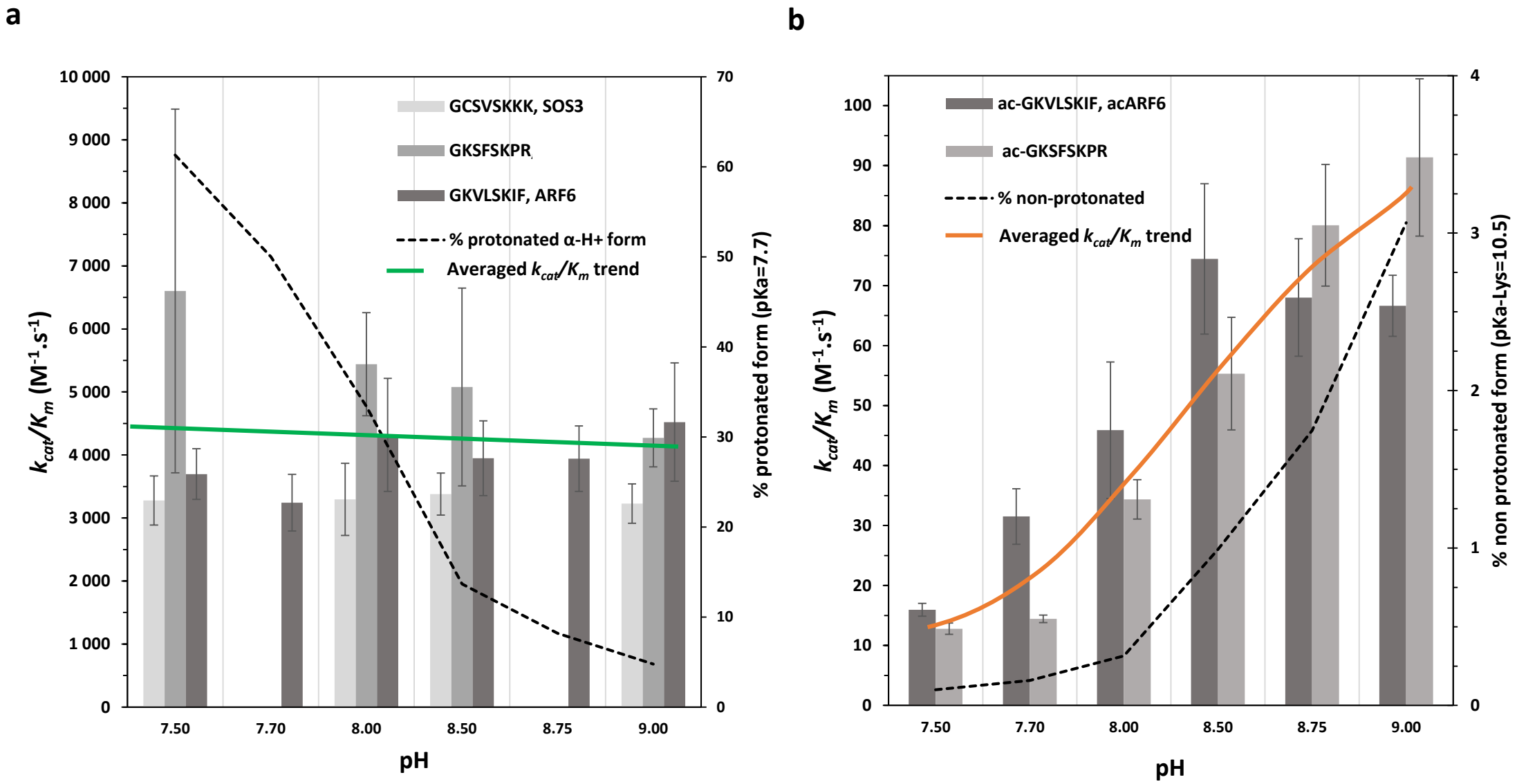
a
GCSVSKKK, SOS3
GKSFSKPR
GKVLSKIF, ARF6
% protonated α-H+ form
Averaged k_{cat}/K_m trend
k_{cat}/K_m ($M^{-1}.s^{-1}$)
% protonated form (pKa=7.7)
pH
b
ac-GKVLSKIF, acARF6
ac-GKSFSKPR
% non-protonated
Averaged k_{cat}/K_m trend
k_{cat}/K_m ($M^{-1}.s^{-1}$)
% non protonated form (pKa-Lys=10.5)
pH

Figure 6

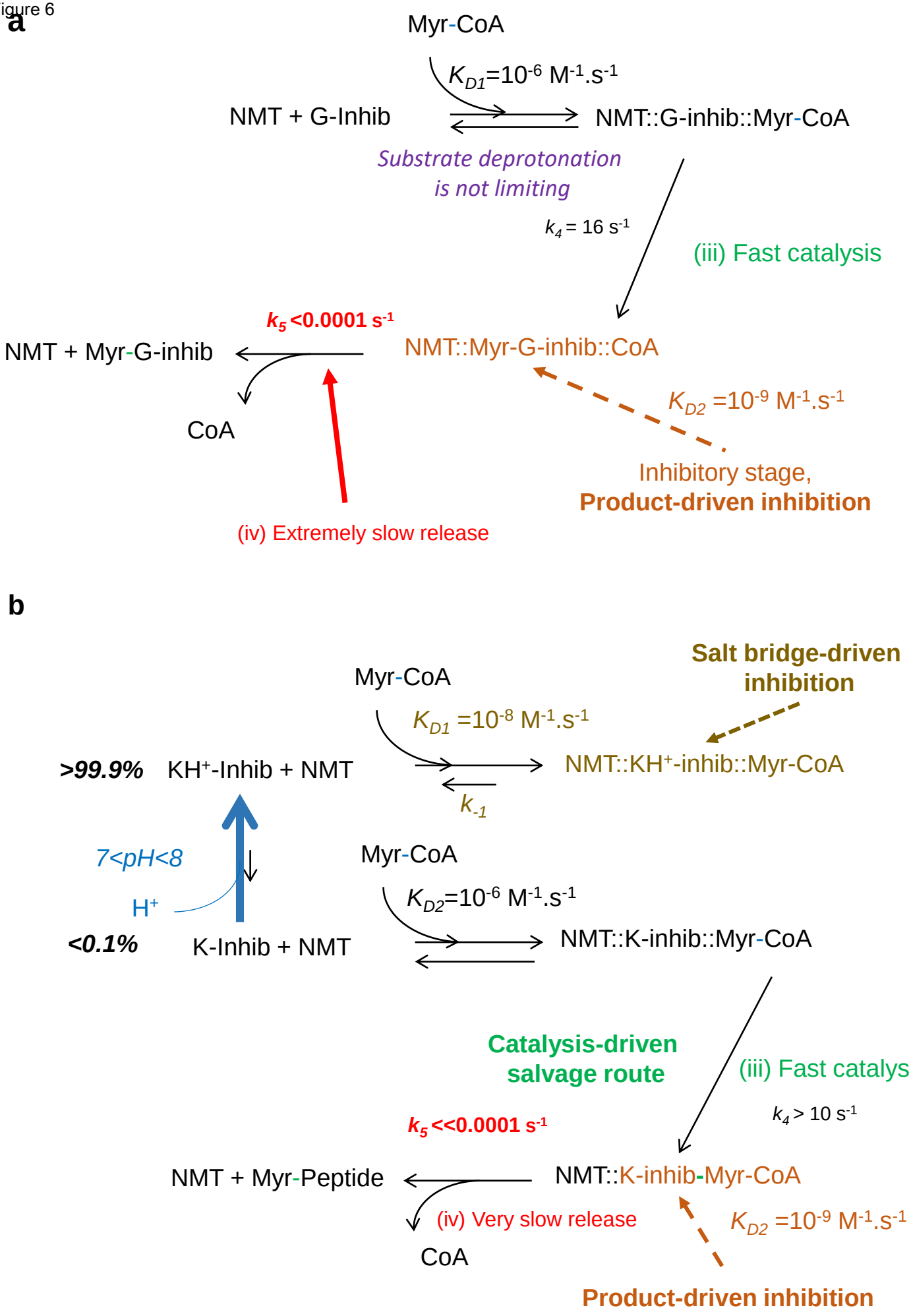

Figure 6

Figure 7

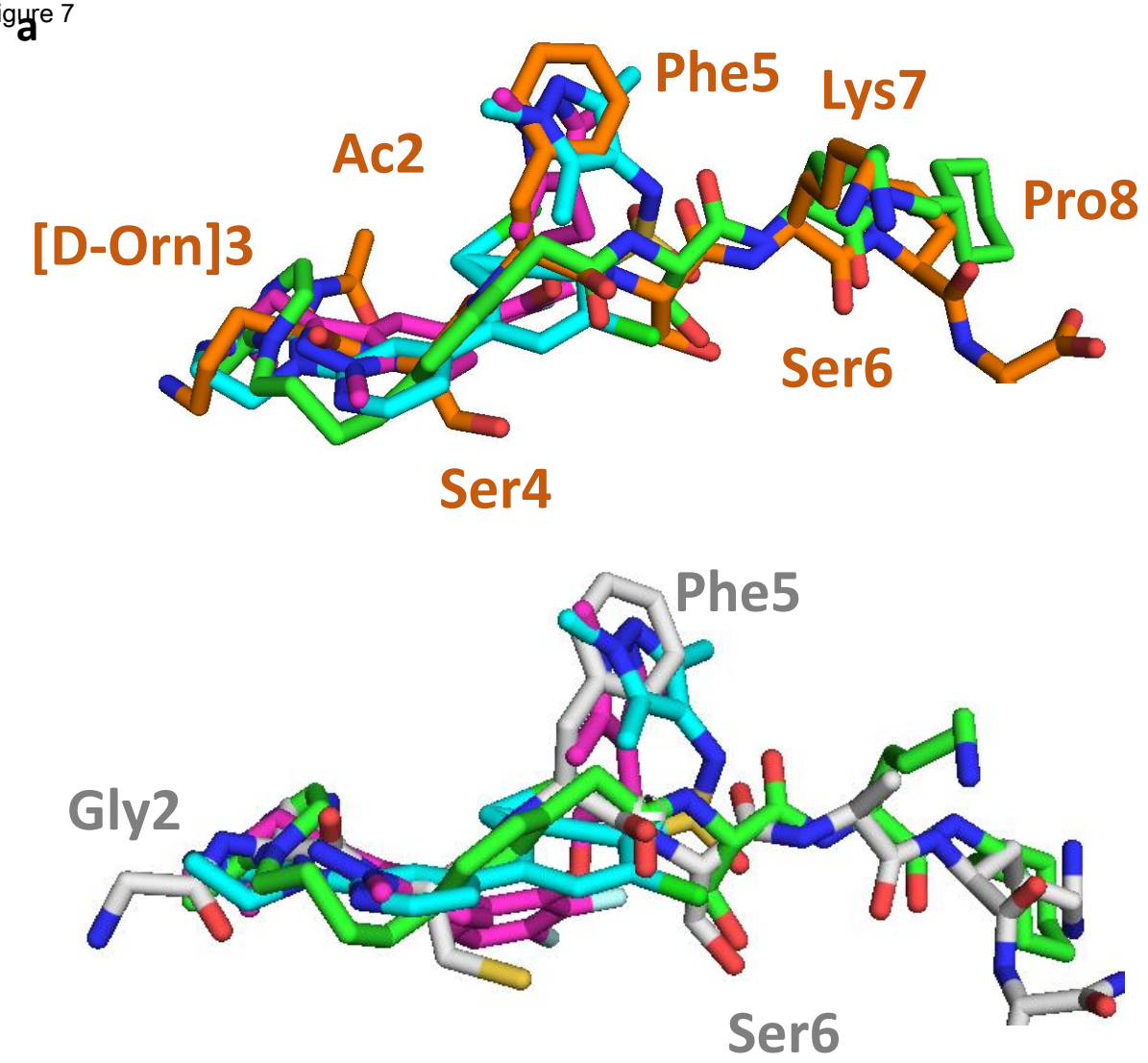

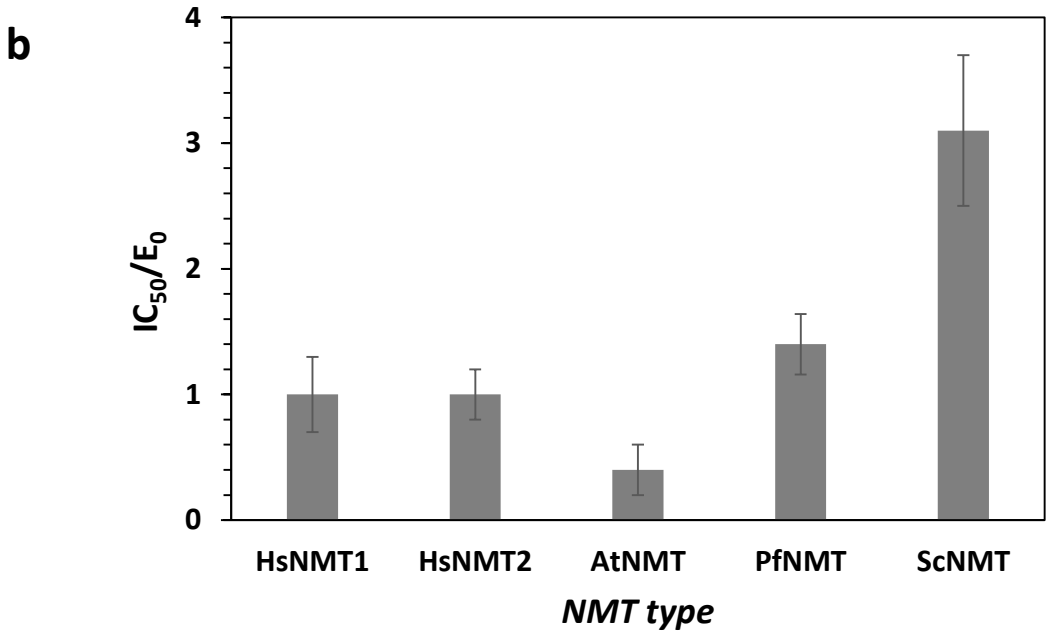

Figure 7